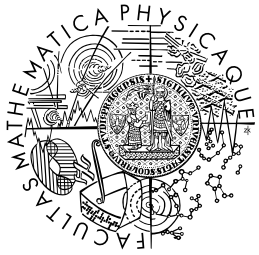

FACULTY
OF MATHEMATICS
AND PHYSICS
Charles University

**BACHELOR THESIS**

Ondřej Kureš

# Motional electromagnetic induction in the subsurface ocean in Europa

Department of Geophysics

Supervisor of the bachelor thesis: doc. RNDr. Jakub Velímský, Ph.D.
Study programme: Mathematical Modelling
Study branch: Mathematics

Prague 2023

I declare that I carried out this bachelor thesis independently, and only with the cited sources, literature and other professional sources. It has not been used to obtain another or the same degree.

I understand that my work relates to the rights and obligations under the Act No. 121/2000 Sb., the Copyright Act, as amended, in particular the fact that the Charles University has the right to conclude a license agreement on the use of this work as a school work pursuant to Section 60 subsection 1 of the Copyright Act.

In ..... date .....  .....

Author's signature

I want to thank my supervisor doc. RNDr. Jakub Velímský, Ph.D., for all the help, guidance and limitless patience. Also, I would like to thank doc. RNDr. Marie Běhounková, Ph.D., for her assistance and initial nudge towards the study of Europa.

Title: Motional electromagnetic induction in the subsurface ocean in Europa

Author: Ondřej Kureš

Department: Department of Geophysics

Supervisor: doc. RNDr. Jakub Velímský, Ph.D., Department of Geophysics

Abstract: Europa is one of the Jovian icy moons with confirmed subsurface ocean. Circulation of the ocean in presence of the Jovian ambient magnetic field leads to generation of the ocean-induced magnetic field (OIMF). On Earth, the OIMF has potential to provide us with informations about water flow and electrical conductivity. However, the OIMF in Europa has been addressed only briefly in the available literature. This thesis is focused on numerical modelling of motionally driven process of the electromagnetic induction (EMI) in the subsurface ocean of Europa. Firstly, the EMI equation is introduced with its corresponding weak formulation. Its solutions are obtained by the means of finite element method (FEM) in combination with spherical harmonic functions. I discuss the structure of the linear problem and subroutines applied in the numerical solver. The code is successfully tested against a set of independent semi-analytical solutions. Three models of flow in the Europa's ocean are explored, using simple analytical expressions of ocean velocities and Jovian magnetic field.

Keywords: electromagnetic induction, Europa, subsurface ocean

# Contents

# Introduction

Europa is one of the Jovian satellites, more specifically one of the Galilean moons. What makes Europa interesting and worth our attention? Alongside with Callisto and Ganymede, Europa has liquid water in the form of global $\approx$ 100 km thick subsurface ocean, which is expected to be turbulent (Soderlund et al. [2014]). Furthermore, this ocean is probably chemically rich and relatively warm, because of the black smokers at the mantle–ocean boundary. From these assumptions, Europa can be very promising candidate to host life (Blanc et al. [2020]).

The presence of dissociated salts in the subsurface ocean implies its relatively high electrical conductivity. Therefore, the moon has significant inductive response to the time variations of the ambient Jovian magnetic field as it moves along its orbit. Indeed, the magnetic field measurements by the Galileo interplanetary probe were used to detect the presence of the subsurface ocean in Europa (Khurana et al. [1998]).

The flow of conductive water in the presence of ambient magnetic field induces electrical currents in the ocean which in turn generate the ocean–induced magnetic field (OIMF). From observations on Earth, it is known that OIMF provides valuable information on flow and electrical conductivity (Grayver et al. [2017], Velímský et al. [2021]). In this moment we have very little information regarding magnetic field of Europa, but new data will be brought by two space missions: the NASA's Europa Clipper and the ESA's JUICE in early 2030s.

So far, the generation of OIMF in Europa has been addressed only by (Vance et al. [2021]). However, in their study, the solution of the electromagnetic induction (EMI) equation is avoided, and the estimates of OIMF are based only on a scaling analysis. Under this simplification, they predict the OIMF strength of approximately 20 nT - a value potentially observable by modern magnetometers on board of interplanetary probes. An obvious next step, which is the topic of this thesis, is to apply the EMI equation to obtain physically consistent predictions of the Europa's OIMF. A numerical solver of the time-domain EMI equation with internal motional forcing is thus developed, tested, and subsequently applied to a series of scenarios, using various electrical conductivity profiles (Vance et al. [2021]), and elementary geometrical structures of the ocean flow.

In the first chapter, I formulate the problem of motional electromagnetic induction in the subsurface ocean and introduce the numerical methods, which are used. Formulation and numerical solution is based on the work of my supervisor (Velímský and Martinec [2005]), but reimplemented in python programming language.

In the second chapter, I take closer look on the system of linear equations stemming from the numerical methods and the numerical solver.

The third chapter is focused on testing of the code against two semi-analytical solutions.

In the fourth chapter I introduce the conductivity profiles of Europa's interior, and simplified models of the ocean flow. The predicted OIMFs are presented and discussed in the final chapter.

# 1. Electromagnetic induction equation with motional forcing

## 1.1 Classical and integral formulation

We use the spherical coordinates $\mathbf{r} = (r, \vartheta, \varphi)$, where $r, \vartheta$ and $\varphi$ stand for radius, colatitude and longitude. Europa is represented by a spherical domain $G$ with outer boundary $\partial G$ at $r = R_E$, where $R_E$ is the diameter of Europa, and the outer normal is $\mathbf{e}_r$.

### 1.1.1 Classical formulation

To formulate the EMI equation, the quasi–static approximation of the Maxwell equations is used, namely

$$\nabla \times \mathbf{B} = \mu_0 \mathbf{j} \qquad \ldots\ldots \qquad \text{Ampère's law,} \tag{1.1}$$

$$\nabla \times \mathbf{E} = -\frac{\partial \mathbf{B}}{\partial t} \qquad \ldots\ldots \qquad \text{Faraday's law,} \tag{1.2}$$

$$\mathbf{j} = \sigma \left( \mathbf{E} + \mathbf{u} \times \mathbf{B} \right) \qquad \ldots\ldots \qquad \text{Ohm's law,} \tag{1.3}$$

where $\mathbf{B}(\mathbf{r}; t), \mathbf{E}(\mathbf{r}; t), \mathbf{j}(\mathbf{r}; t), \sigma(\mathbf{r}; t)$ and $\mathbf{u}(\mathbf{r}; t)$ denote the magnetic flux density, electric field, free current density, electrical conductivity and the velocity, which is non–zero only in the ocean layer. Generally, the electrical conductivity $\sigma(\mathbf{r}; t)$ can vary both in space and time, but in this work, only 1–D, radially dependent conductivity models $\sigma(r)$ without time variation are used.

By combining equations (1.1–1.3), the general EMI equation is obtained

$$\mu_0 \frac{\partial \mathbf{B}}{\partial t} + \nabla \times \left( \frac{1}{\sigma} \nabla \times \mathbf{B} \right) = \mu_0 \nabla \times (\mathbf{u} \times \mathbf{B}) \,. \tag{1.4}$$

The equation (1.4) implicitly satisfies Gauss's law

$$\nabla \cdot \mathbf{B} = \mathbf{0}. \tag{1.5}$$

Using $\mathbf{B} \to \mathbf{B} + \mathbf{B}_J$, where $\mathbf{B}$ is the motionally induced magnetic field and $\mathbf{B}_J$ is the ambient Jovian magnetic field, yields the EMI equation

$$\mu_0 \frac{\partial \mathbf{B}}{\partial t} + \nabla \times \left( \frac{1}{\sigma} \nabla \times \mathbf{B} \right) = \mu_0 \nabla \times \mathbf{L} - \mu_0 \frac{\partial \mathbf{B}_J}{\partial t}, \tag{1.6}$$

where $\mathbf{L}(\mathbf{r}; t) = \mathbf{u}(\mathbf{r}; t) \times \mathbf{B}_J(\mathbf{r}; t)$ is the imposed electric field caused by the Lorentz force action of the Jovian field on the moving charge carriers in the saltwater ocean. For fields $\mathbf{B}$ and $\mathbf{B}_J$ holds $|\mathbf{B}| \ll |\mathbf{B}_J|$ and the Jovian magnetic field can be expressed by a magnetic potential, $\mathbf{B}_J = -\nabla U_J$.

The boundary and initial conditions for (1.6) are

$$\mathbf{B}^{(ext)}(\mathbf{r}; t) = \mathbf{0}|_{\partial G}, \qquad \mathbf{B}(\mathbf{r}; 0) = \mathbf{B}_0(\mathbf{r}). \tag{1.7}$$

$\mathbf{B}^{(ext)}(\mathbf{r}; t)$ is the external part of magnetic field, generated by electric currents outside the conductor. This is a short formulation, where the magnetic field in

the insulating surroundings of the moon can be represented by scalar magnetic potential $U(\mathbf{r};t)$, so that $\mathbf{B} = -\nabla U|_{\partial G}$, $\Delta U = 0$ for $r \geq R_E$ and $U \approx \mathcal{O}(\frac{1}{r^2})$ as $r \to \infty$. The modelling of the EMI excited by time variations of the external field is outside of the scope of this thesis. However, the externally induced magnetic field and the OIMF are additive.

### 1.1.2 Integral (weak) formulation

Multiplying (1.6) by an arbitrary test function $\delta\mathbf{B}$ and integrating over $G$ yields

$$\mu_0 \int_G \frac{\partial \mathbf{B}}{\partial t} \cdot \delta\mathbf{B} dV + \int_G \nabla \times \left(\frac{1}{\sigma}\nabla \times \mathbf{B}\right) \cdot \delta\mathbf{B} dV = \mu_0 \int_G (\nabla \times \mathbf{L}) \cdot \delta\mathbf{B} dV - \mu_0 \int_G \frac{\partial \mathbf{B}_J}{\partial t} \cdot \delta\mathbf{B} dV. \quad (1.8)$$

The Green theorem for rotation operators and sufficiently smooth functions $h(\mathbf{r})$, $\mathbf{f}(\mathbf{r})$, and $\mathbf{g}(\mathbf{r})$ reads as

$$\int_G \nabla \times (h\nabla \times \mathbf{f}) \cdot \mathbf{g} dV = \int_G h\,(\nabla \times \mathbf{f}) \cdot (\nabla \times \mathbf{g})\, dV - \int_{\partial G} h\,(\nabla \times \mathbf{f}) \cdot (\vec{e}_r \times \mathbf{g})\, dS. \quad (1.9)$$

Application of the Green theorem to equation (1.8) yields the integral formulation of the EMI equation,

$$\mu_0 \int_G \frac{\partial \mathbf{B}}{\partial t} \cdot \delta\mathbf{B} dV + \int_G \frac{1}{\sigma} (\nabla \times \mathbf{B}) \cdot (\nabla \times \delta\mathbf{B})\, dV = = \mu_0 \int_G (\nabla \times \delta\mathbf{B}) \cdot \mathbf{L} dV - \mu_0 \int_G \frac{\partial \mathbf{B}_J}{\partial t} \cdot \delta\mathbf{B} dV. \quad (1.10)$$

Let $\mu_0 > 0$ be the magnetic permeability, $\sigma(r) \in \mathcal{L}^+_\infty(\bar{R}, \mathbb{R}) \cap C^0(\bar{R})$ the electrical conductivity, where $\bar{R} =< 0, R_E >$, $\mathbf{B}_J(\mathbf{r};t) \in C^1(\bar{I}; \mathcal{L}_2(G, \mathbb{R}^3))$ the Jovian magnetic field and $\mathbf{L}(\mathbf{r};t) \in C^0(\bar{I}; \mathcal{L}_2(G, \mathbb{R}^3))$ the imposed electric field, where $\bar{I} =< t_0, t_1 >$. Let $\mathbf{B}_0(\mathbf{r}) \in V_{0T}$ be the initial condition, at $t_0 = 0$. We want to find solution $\mathbf{B}(\mathbf{r};t) \in C^1(\bar{I}; V_{0T})$ which solves (1.10), $\forall \delta\mathbf{B}(\mathbf{r}) \in V_0$ and $\forall t \in I$. Functional spaces are defined in Table 1.1. The boundary condition takes the form

$$\int_{\partial G} \left[\mathbf{S}^{(-1)}_{jm} + \frac{1}{j}\mathbf{S}^{(1)}_{jm}\right] \cdot \mathbf{B} dS = 0, \quad (1.11)$$

$\forall j = 1, 2, \ldots, \infty$, $m = -j, \ldots, 0, \ldots, +j$ and $\forall t \in I$. This is the external boundary condition and will be discussed in subsection 1.2.1. The spherical harmonic vectors $\mathbf{S}^{(-1)}_{jm}$ and $\mathbf{S}^{(1)}_{jm}$ are defined in appendix A.2.

## 1.2 Problem discretization

For the numerical solution we use a combination of finite element parameterization in the radial coordinate, and spherical harmonic functions (SHF) in the lateral coordinates. The respective definitions and properties are included in Appendices A.3 and A.2.

Table 1.1: Definitions of functional spaces. The toroidal–poloidal decomposition of a divergence-free vector field, which is used in the definitions of functional spaces, is recalled in appendix A.1.

| | |
|---|---|
| $C^0\left(\bar{R};\mathbb{R}\right)$ | real scalar functions continuous on the interval $\bar{R}$. |
| $\mathcal{L}^+_\infty(\bar{R},\mathbb{R})$ | real scalar positive functions bounded on the interval $\bar{R}$. |
| $\mathcal{L}_2(G,\mathbb{R}^3)$ | real vector functions, square–integrable in $G$. Scalar product $(\mathbf{f},\mathbf{g})_{\mathcal{L}_2} = \int_G \mathbf{f}\cdot\mathbf{g}dV$ is generating norm $\|\mathbf{f}\|_{\mathcal{L}_2} = \sqrt{(\mathbf{f},\mathbf{f})}_{\mathcal{L}_2}$. |
| $H_{\mathrm{curl}}$ | real vector functions $\mathbf{f}\in\mathcal{L}_2(G,\mathbb{R}^3)$ such that $\nabla\times\mathbf{f}\in\mathcal{L}_2(G,\mathbb{R}^3)$. Scalar product $(\mathbf{f},\mathbf{g})_{H_{\mathrm{curl}}} = \int_G (\mathbf{f}\cdot\mathbf{g}+(\nabla\times\mathbf{f})\cdot(\nabla\times\mathbf{g}))\,dV$ is generating norm $\|\mathbf{f}\|_{H_{\mathrm{curl}}} = \sqrt{(\mathbf{f},\mathbf{f})}_{H_{\mathrm{curl}}}$. |
| $H_{\mathrm{curl},0}$ | real vector functions $\mathbf{f}\in H_{\mathrm{curl}}$ such that $\mathbf{e}_r\times\mathbf{f}=\mathbf{0}$ on $\partial G$. |
| $H_{\mathrm{curl},0T}$ | real vector functions $\mathbf{f}\in H_{\mathrm{curl}}$ such that $\mathbf{e}_r\times\mathbf{f}_T=\mathbf{0}$ on $\partial G$, where $\mathbf{f}_T$ is the toroidal part of $\mathbf{f}$. |
| $H^0_{\mathrm{div}}$ | real vector functions $\mathbf{f}\in\mathcal{L}_2(G,\mathbb{R}^3)$ such that $\nabla\cdot f=0$ in $G$. |
| $V_0$ | real vector functions $\mathbf{f}\in H_{\mathrm{curl},0}\cap H^0_{\mathrm{div}}$. |
| $V_{0T}$ | real vector functions $\mathbf{f}\in H_{\mathrm{curl},0T}\cap H^0_{\mathrm{div}}$. |
| $C^n(\bar{I};S)$ | space of all mappings from the closed time interval $\bar{I}=<t_0,t_1>$ to a functional space $S$, continuous up to the $n$–th derivative with respect to time. |

### 1.2.1 Spherical harmonic expansions

The spherical harmonic functions provide very powerful tool for solving partial differential equations in spherical coordinates. The magnetic field $\mathbf{B}(\mathbf{r};t)$ can be expressed in the vector spherical harmonic basis

$$\mathbf{B}(\mathbf{r};t) = \sum_{j=1}^{\infty}\sum_{m=-j}^{j}\sum_{\lambda=-1}^{1} B^{(\lambda)}_{jm}(r;t)\mathbf{S}^{(\lambda)}_{jm}(\Omega). \tag{1.12}$$

Note that the term $(j,m)=(0,0)$ in the spherical harmonic expansion is omitted, as it would correspond to a magnetic field generated by a monopole, in contradiction to the Gauss law (1.5). The vectors $\delta\mathbf{B}$, $\mathbf{B}_J$ and $\mathbf{L}$ are expressed in the same way.

As introduced in subsection 1.1.1, the boundary condition

$$\mathbf{B}^{(ext)}(\mathbf{r};t) = \mathbf{0}|_{\partial G} \tag{1.13}$$

is defined by the continuity of the magnetic field across the boundary $\partial G$

$$\mathbf{B} = -\nabla U|_{\partial G}, \tag{1.14}$$

where the scalar magnetic potential $U(\mathbf{r};t)$ is an analytical solution for the Laplace equation $\Delta U = 0$ for $r \geq R_E$, in the absence of external sources of magnetic field. This analytical solution can be written as a series of scalar spherical harmonic functions $Y_{jm}(\Omega)$,

$$U(\mathbf{r};t) = R_E\sum_{jm}\left[G^{(e)}_{jm}(t)\left(\frac{r}{R_E}\right)^j + G^{(i)}_{jm}(t)\left(\frac{R_E}{r}\right)^{j+1}\right]Y_{jm}(\Omega). \tag{1.15}$$

The coefficients $G_{jm}^{(i)}(t)$ and $G_{jm}^{(e)}(t)$ represent the internal and external field, respectively. By using property (A.14) we obtain

$$\nabla U = \sum_{jm} \left[ jG_{jm}^{(e)}(t) \left( \frac{r}{R_E} \right)^{j-1} - (j+1)G_{jm}^{(i)}(t) \left( \frac{R_E}{r} \right)^{j+1} \right] \mathbf{S}_{jm}^{(-1)} + \\ + \sum_{jm} \left[ G_{jm}^{(e)}(t) \left( \frac{r}{R_E} \right)^{j-1} + G_{jm}^{(i)}(t) \left( \frac{R_E}{r} \right)^{j+1} \right] \mathbf{S}_{jm}^{(1)},$$

and due to (1.12) and (1.14) the coefficients of $\mathbf{B}$ at $r = R_E$ then satisfy

$$\begin{aligned} B_{jm}^{(0)}(R_E;t) &= 0, \\ B_{jm}^{(-1)}(R_E;t) &= -\left[ jG_{jm}^{(e)}(t) - (j+1)G_{jm}^{(i)}(t) \right], \\ B_{jm}^{(1)}(R_E;t) &= -\left[ G_{jm}^{(e)}(t) + G_{jm}^{(i)}(t) \right]. \end{aligned}$$

By eliminating $G_{jm}^{(i)}(t)$, we obtain

$$B_{jm}^{(0)}(a;t) = 0, \tag{1.16}$$

$$B_{jm}^{(-1)}(a;t) + (j+1)B_{jm}^{(1)}(a;t) = -(2j+1)G_{jm}^{(e)}(t), \tag{1.17}$$

where $G_{jm}^{(e)}(t) = 0$ in the absence of external fields. Using the orthogonality of spherical harmonic functions, the boundary condition (1.17) is equivalently expressed by an infinite set of integral conditions

$$\int_{\partial G} \left[ \mathbf{S}_{jm}^{(-1)} + \frac{1}{j} \mathbf{S}_{jm}^{(1)} \right] \cdot \mathbf{B} dS = 0, \tag{1.18}$$

$\forall j = 1, \ldots, \infty$ and $m = -j, \ldots, 0, \ldots, j$. However, condition (1.17) is preferred, as it can be directly applied to the construction of the discretization of the functional space $V_{0T}$.

Divergence–free condition $\nabla \cdot \mathbf{B} = \mathbf{0}$ must be fulfilled, but due to the properties of the spherical harmonic vectors, as we can see in equations (A.15–A.17), only the toroidal components satisfy this condition implicitly. However, by the means of the Lagrange multipliers we can suppress the divergence of the poloidal–scaloidal components. In order to do that, the penalty term

$$\int_G \left[ \delta\Lambda(\nabla \cdot \mathbf{B}) + \Lambda(\nabla \cdot \delta\mathbf{B}) \right] dV \tag{1.19}$$

is added to the left–hand side of integral formulation. $\Lambda(\mathbf{r};t)$ is expanded into scalar spherical harmonic functions

$$\Lambda(\mathbf{r};t) = \sum_{j=1}^{\infty} \sum_{m=-j}^{j} \Lambda_{jm}(r;t) Y_{jm}(\Omega), \tag{1.20}$$

and similarly for $\delta\Lambda(\mathbf{r};t)$.

### 1.2.2 Finite element method

Following the expansion of $\mathbf{B}(\mathbf{r};t)$ into the vector spherical harmonic basis, we introduce the radial discretization using piecewise linear elements, as defined in equation (A.21),

$$B_{jm}^{(\lambda)}(r;t) = \sum_{k=1}^{k_{max+1}} B_{jm}^{(\lambda,k)}(t)\psi_k(r). \tag{1.21}$$

Similar expansion is used also for the test functions $\delta\mathbf{B}$.

The boundary conditions (1.16–1.17) have the discrete form

$$B_{jm}^{(0,k_{max+1})} = 0, \tag{1.22}$$

$$B_{jm}^{(-1,k_{max+1})} + (j+1)B_{jm}^{(1,k_{max+1})} = 0. \tag{1.23}$$

The coefficients $L_{jm}^{(\lambda)}(r;t), \Lambda_{jm}(r;t)$ and the electrical conductivity $\sigma(r)$ are represented by piecewise constant functions $\xi_k$, defined in equation (A.22),

$$L_{jm}^{(\lambda)}(r;t) = \sum_{k=1}^{k_{max}} L_{jm}^{(\lambda,k)}(t)\xi_k(r), \tag{1.24}$$

$$\Lambda_{jm}(r;t) = \sum_{k=1}^{k_{max}} \Lambda_{jm}^{(k)}(t)\xi_k(r), \tag{1.25}$$

$$\sigma(r) = \sum_{k=1}^{k_{max}} \sigma_k\xi_k(r). \tag{1.26}$$

### 1.2.3 Assembly of the linear problem

Using relations from subsection 1.2.1 and 1.2.2, discretization of the integral formulation gives us the left–hand side terms,

$$\mu_0\int_G \frac{\partial\mathbf{B}}{\partial t}\cdot\delta\mathbf{B}dV = \mu_0\sum_{jm}\sum_{kk'} I_{kk'}\Big[\delta B_{jm}^{(-1,k)}\dot{B}_{jm}^{(-1,k')} + \\ +j(j+1)\delta B_{jm}^{(0,k)}\dot{B}_{jm}^{(0,k')} + j(j+1)\delta B_{jm}^{(1,k)}\dot{B}_{jm}^{(1,k')}\Big], \tag{1.27}$$

$$\int_G \frac{1}{\sigma}\left(\nabla\times\mathbf{B}\right)\cdot\left(\nabla\times\delta\mathbf{B}\right)dV = \sum_{jm}\sum_{kk'} j(j+1)\Big[\delta B_{jm}^{(-1,k)}B_{jm}^{(-1,k')}K_{kk'}^{(1)} - \\ -\delta B_{jm}^{(1,k)}B_{jm}^{(-1,k')}K_{kk'}^{(3)} - \delta B_{jm}^{(-1,k)}B_{jm}^{(1,k')}K_{kk'}^{(4)} + \delta B_{jm}^{(1,k)}B_{jm}^{(1,k')}K_{kk'}^{(2)} + \\ +\delta B_{jm}^{(1,k)}B_{jm}^{(1,k')}K_{kk'}^{(2)} + \delta B_{jm}^{(0,k)}B_{jm}^{(0,k')}\Big[j(j+1)K_{kk'}^{(1)} + K_{kk'}^{(2)}\Big]\Big], \tag{1.28}$$

and the right–hand side,

$$\mu_0\int_G \left(\nabla\times\delta\mathbf{B}\right)\cdot\mathbf{L}dV = \mu_0\sum_{jm}\sum_{kk'} j(j+1)\Big[-\delta B_{jm}^{(-1,k)}L_{jm}^{(0,k')}\Theta_{kk'}^{(2)} + \\ +\delta B_{jm}^{(1,k)}L_{jm}^{(0,k')}\Theta_{kk'}^{(4)} - \delta B_{jm}^{(0,k)}\left(L_{jm}^{(-1,k')}\Theta_{kk'}^{(2)} + L_{jm}^{(1,k')}\Theta_{kk'}^{(4)}\right)\Big], \tag{1.29}$$

$$\mu_0 \int_G \frac{\partial \mathbf{B}_J}{\partial t} \cdot \delta\mathbf{B} dV = \mu_0 \sum_{jm} \sum_{kk'} I_{kk'} \Big[ \delta B_{jm}^{(-1,k)} \dot{B}_{J,jm}^{(-1,k')} + \\ + j(j+1) \delta B_{jm}^{(0,k)} \dot{B}_{J,jm}^{(0,k')} + j(j+1) \delta B_{jm}^{(1,k)} \dot{B}_{J,jm}^{(1,k')} \Big]. \quad (1.30)$$

The penalty term (1.19) takes the form

$$\int_G \left[ \delta\Lambda (\nabla \cdot \mathbf{B}) + \Lambda (\nabla \cdot \delta\mathbf{B}) \right] dV = \sum_{jm} \sum_{kk'} \Big[ \delta\Lambda_{jm}^{(k)} B_{jm}^{(-1,k')} \Theta_{kk'}^{(5)} - \\ - j(j+1) \delta\Lambda_{jm}^{(k)} B_{jm}^{(1,k')} \Theta_{kk'}^{(1)} + \Lambda_{jm}^{(k')} \delta B_{jm}^{(-1,k)} \Theta_{kk'}^{(6)} - j(j+1) \Lambda_{jm}^{(k')} \delta B_{jm}^{(1,k)} \Theta_{kk'}^{(2)} \Big]. \quad (1.31)$$

A list of integrals $I, K, \Theta$ with their values is found in Appendix A.4.

The Galerkin discretization gives us a system of ordinary equations

$$M_1 \cdot \frac{\partial \mathbf{x}(t)}{\partial t} + M_2 \cdot \mathbf{x}(t) = \mathbf{b}(t). \quad (1.32)$$

Thanks to 1-D (radial) conductivity, equation (1.32) is solved separately for each combination of spherical harmonic degree $j$ and order $m$, and for the toroidal and poloidal part. The penalty term (1.19) is present only in the poloidal part. Matrices $M_1$ and $M_2$, the solution vector $\mathbf{x}(t)$ and the right hand side vector $\mathbf{b}(t)$ in the toroidal part have different structures than their counterparts in the poloidal part, as discussed in next chapter.

The equation (1.32) is solved implicitly, with time derivative approximation

$$\frac{\partial \mathbf{x}(t)}{\partial t} \approx \frac{{}^{i+1}\mathbf{x} - {}^{i}\mathbf{x}}{\Delta t}. \quad (1.33)$$

Hence, the time integration scheme is written as

$$\left( \frac{1}{\Delta t} M_1 + M_2 \right) {}^{i+1}\mathbf{x} = \frac{1}{\Delta t} M_1 {}^{i}\mathbf{x} + {}^{i+1}\mathbf{b}, \quad (1.34)$$

where ${}^{i}\mathbf{x}$ and ${}^{i}\mathbf{b}$ relate to their value at the time level $t_i = t_0 + i\Delta t$.

# 2. Numerical solver

My goal is to solve repeatedly for each time step a system of linear equations

$$A\mathbf{x} = \mathbf{y}, \tag{2.1}$$

where $A$ is an $N \times N$ matrix and vectors $\mathbf{x},\ \mathbf{y}$ have dimension $N$, for each degree $j$ and order $m$.

## 2.1 Toroidal part ($\lambda = 0$)

Vector $\mathbf{x}$ has structure

$$\mathbf{x} = \left({}^{i+1}B_{jm}^{(0,1)}, \ldots, {}^{i+1}B_{jm}^{(0,k_{max}+1)}\right) \tag{2.2}$$

$A_{tor}$ is a tridiagonal symmetric matrix, $N = k_{max}+1$. The individual components are

$$a_{kk'} = \frac{1}{\Delta t}\mu_0 j(j+1) I_{kk'} + j(j+1)\left[j(j+1)K_{kk'}^{(1)} + K_{kk'}^{(2)}\right]. \tag{2.3}$$

It depends only on the spherical harmonic degree $j$, the radial conductivity model, the radial discretization, and the time step $\Delta t$.

The right hand–side vector has structure

$$\mathbf{y} = \left(y_1, \ldots, y_{k_{max}+1}\right), \tag{2.4}$$

where the individual components are described as

$$y_k = \mu_0 j(j+1) \sum_{k'=k-1}^{k+1} \Big[\frac{1}{\Delta t} I_{kk'} \left({}^{i}B_{jm}^{(0,k')} - {}^{i+1}B_{J,jm}^{(0,k')} + {}^{i}B_{J,jm}^{(0,k')}\right) - \\ - {}^{i+1}L_{jm}^{(-1,k')}\Theta_{kk'}^{(2)} - {}^{i+1}L_{jm}^{(1,k')}\Theta_{kk'}^{(4)}\Big]. \tag{2.5}$$

The boundary condition

$$B_{jm}^{(0,k_{max}+1)} = 0 \tag{2.6}$$

needs to be accounted for. This is done by making the last row of matrix $A_{tor}$ only zeros except the last element, which I set to one, and setting $y_{k_{max}+1} = 0$.

## 2.2 Poloidal part ($\lambda = -1, 1$)

Vector $\mathbf{x}$ has structure

$$\mathbf{x}(t) = \left(\left\{\left[{}^{i+1}B_{jm}^{(\lambda,k)}\right]_{\lambda=-1,1}, {}^{i+1}\Lambda_{jm}^{(k)}\right\}_{k=1}^{k_{max+1}}\right). \tag{2.7}$$

$A_{pol}$ is a block–tridiagonal symmetric matrix, $N = 3(k_{max}+1)$. The individual $3 \times 3$ blocks are

$$A_{kk'} = \begin{pmatrix} \mu_0 I_{kk'} + j(j+1)K_{kk'}^{(1)} & -j(j+1)K_{kk'}^{(4)} & \Theta_{kk'}^{(6)} \\ -j(j+1)K_{kk'}^{(3)} & j(j+1)\left[\mu_0 I_{kk'} + K_{kk'}^{(2)}\right] & -j(j+1)\Theta_{kk'}^{(2)} \\ \Theta_{kk'}^{(5)} & -j(j+1)\Theta_{kk'}^{(1)} & 0 \end{pmatrix}.$$

It also depends on the spherical harmonic degree $j$, the discretized conductivity profile, and the time step $\Delta t$.

The right hand–side vector has structure

$$\mathbf{y} = \left( \left\{ \gamma_k^{(-1)}, \gamma_k^{(1)}, 0 \right\}_{k=1}^{k_{max}+1} \right), \tag{2.8}$$

where the first component is described as

$$\gamma_k^{(-1)} = \mu_0 \sum_{k'=k-1}^{k+1} \Big[ \frac{1}{\Delta t} I_{kk'} \left( {}^{i}B_{jm}^{(-1,k')} - {}^{i+1}B_{J,jm}^{(-1,k')} + {}^{i}B_{J,jm}^{(-1,k')} \right) - \\ - j(j+1) L_{jm}^{(0,k')} \Theta_{kk'}^{(2)} \Big], \tag{2.9}$$

and the second one as

$$\gamma_k^{(1)} = \mu_0 j(j+1) \sum_{k'=k-1}^{k+1} \Big[ \frac{1}{\Delta t} I_{kk'} \left( {}^{i}B_{jm}^{(1,k')} - {}^{i+1}B_{J,jm}^{(1,k')} + {}^{i}B_{J,jm}^{(1,k')} \right) + \\ + L_{jm}^{(0,k')} \Theta_{kk'}^{(4)} \Big]. \tag{2.10}$$

As in the toroidal part, the boundary condition is enforced by including the constraint

$$B_{jm}^{(-1,k_{max}+1)} + (j+1) B_{jm}^{(1,k_{max}+1)} = 0 \tag{2.11}$$

in the linear system. The Lagrange multiplier $\Lambda$ equals to 0 in the uppermost layer.

Setting for $k = k_{max} + 1, k' = k_{max}$

$$A_{kk'} = \begin{pmatrix} \mu_0 I_{kk'} + j(j+1) K_{kk'}^{(1)} & -j(j+1) K_{kk'}^{(4)} & \Theta_{kk'}^{(6)} \\ 0 & 0 & 0 \\ 0 & 0 & 0 \end{pmatrix},$$

for $k = k_{max} + 1, k' = k_{max} + 1$

$$A_{kk'} = \begin{pmatrix} \mu_0 I_{kk'} + j(j+1) K_{kk'}^{(1)} & -j(j+1) K_{kk'}^{(4)} & 0 \\ 1 & j+1 & 0 \\ 0 & 0 & 1 \end{pmatrix}$$

, and $\gamma_{k_{max}+1}^{(1)} = 0$, we achieve desired result.

## 2.3 Code

The numerical solver is written in *Python 3.8.10*. The respective systems of linear equations for the toroidal and poloidal part are solved by python–imported LAPACK subroutines, see Table 2.1.

The matrices $A_{tor}$ and $A_{pol}$ are only dependent on time step $\Delta t$. Hence, a LU factorization, which for tridiagonal and banded matrices has computational cost of $\mathcal{O}(N^2)$, is calculated only once during the initialization. At each time step only the back–substitution is performed at the cost of $\mathcal{O}(N)$.

Table 2.1: LAPACK subroutines

| | |
|---|---|
| *dgttrf()* | computes an LU factorization of a real tridiagonal matrix $A$. This subroutine is used in toroidal part. Inputs must be diagonal, subdiagonal and superdiagonal of the matrix $A$. |
| *dgttrs()* | solves a system of equations with a tridiagonal matrix $A$ using the LU factorization computed by *dgttrf()*. |
| *dgbtrf()* | computes an LU factorization of a real banded matrix $A$. This subroutine is used in poloidal part. Inputs must be matrix $A$ in banded storage, dimensions in band storage $(2KL+KU+1, N)$, number of subdiagonals $KL$ and number of superdiagonals $KU$. |
| *dgbtrs()* | solves a system of equations with a banded matrix $A$ using the LU factorization computed by *dgbtrf()*. |

# 3. Test against semi–analytical solution

The purpose of the test is to verify the correctness of the problem formulation and its implementation. We assume a 2–layer sphere with the size of the Earth, but with unrealistically deep ocean in the upper layer;

- $b = 5000$ km; radius of inner sphere,
- $\sigma_B = 1$ S/m; conductivity of inner sphere,
- $a = 6371$ km; radius of surface,
- $\sigma_A = 3.5$ S/m; conductivity of the spherical ocean layer.

The EMI equation

$$\mu_0 \frac{\partial \mathbf{B}}{\partial t} + \nabla \times \left( \frac{1}{\sigma} \nabla \times \mathbf{B} \right) = \mu_0 \nabla \times \mathbf{L} \tag{3.1}$$

is reformulated in the frequency domain, assuming the ocean forcing has harmonic time dependence with angular frequency $\omega$,

$$\omega = \frac{2\pi}{T} = \frac{2\pi}{180 \text{ days}}, \tag{3.2}$$

$$-\imath\omega\mu_0 \tilde{\mathbf{B}} + \nabla \times \left( \frac{1}{\sigma} \nabla \times \tilde{\mathbf{B}} \right) = \mu_0 \nabla \times \tilde{\mathbf{L}}, \tag{3.3}$$

where the imposed electric field

$$\tilde{\mathbf{L}} = \tilde{\mathbf{u}} \times \tilde{\mathbf{B}}_0 \tag{3.4}$$

is zonal in the ocean layer. Two separate cases are considered, one for the toroidal part and one for the poloidal part,

$$\tilde{\mathbf{L}} = \sum_{jm} S_{jm} \left( \frac{r}{a} \right)^{j+1} \mathbf{Y}^{j+1}_{jm}, \tag{3.5}$$

$$\tilde{\mathbf{L}} = \sum_{jm} S_{jm} \left( \frac{r}{a} \right)^{j} \mathbf{Y}^{j}_{jm}. \tag{3.6}$$

The complex spherical harmonic vectors $\mathbf{Y}^{j-1}_{jm}$, $\mathbf{Y}^{j}_{jm}$, and $\mathbf{Y}^{j+1}_{jm}$, that are used in the semi–analytical solution, represent an alternative system of orthogonal function to the one defined in A.2. Their definition can be found in (Varshalovich [1989], pages 210–211).

Equation (3.3) has general solution, which is based on the expansion using spherical Bessel functions and a particular solution in the ocean layer, which can be derived analytically for the forcing defined by (3.5) or (3.6). The coefficients of the general solution in both layers are determined numerically by solving a simple linear system defined by the boundary conditions on the inner and outer interfaces of the two-layer model. Full explanation is presented in Appendix A.5.

## 3.1 Test implementation in the time domain

Each test was conducted only for $j = 1, m = 0$. The following settings were used:

- initial condition $\mathbf{B}_0 = \mathbf{0}$
- imposed electric field $\mathbf{L}(t) = 2Re\{\tilde{\mathbf{L}}e^{i\omega t}\}$
- radial discretization of radius 6371 km to 1 km intervals
- $\Delta t = 3600$ s; $t_{max} = 10T$ days $\rightarrow$ number of time steps $t_{max}/\Delta t = 43200$

In order to suppress the transient effect of the initial condition, the solver is run for 10 periods. Results from the last period are transformed into the Fourier domain using the numerical integration

$$\tilde{\mathbf{B}}(\omega) = \frac{1}{T}\int_{9T}^{10T} \mathbf{B}(t)e^{-i\omega t}dt, \tag{3.7}$$

and compared to the analytical solution.

### 3.1.1 Toroidal part

The result of the toroidal field benchmark is shown in Figure 3.1, where a radial dependence of the real and imaginary components of $B_\varphi$ is plotted at fixed colatitude $\vartheta = 140$ degrees. The match between both solutions is perfect, thus demonstrating the correctness of the FEM implementation for the toroidal field.

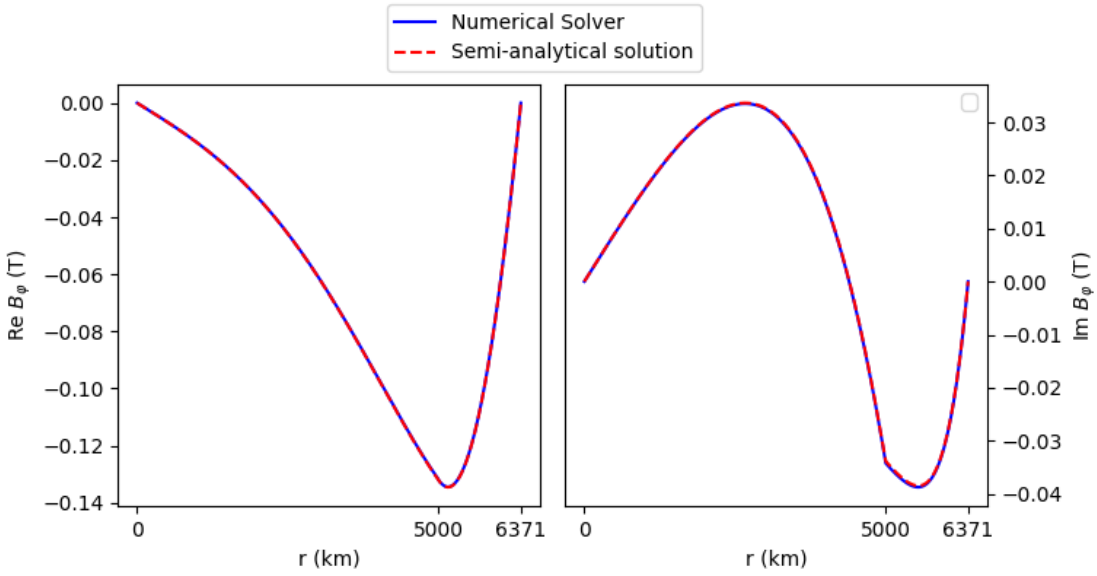


Figure 3.1: Radial depedence of the real and imaginary components $B_\varphi$ at fixed colatitude $\vartheta = 140$ degrees.

### 3.1.2 Poloidal part

The results of the poloidal field benchmark are shown in Figures 3.2 and 3.3, where a radial dependence of the real and imaginary components of $B_r$ and $B_\vartheta$ is plotted at fixed colatitude $\vartheta = 140$ degrees. Both solutions for $B_r$ and $B_\vartheta$ match perfectly, thus demonstrating the correctness of the FEM implementation for the poloidal field.

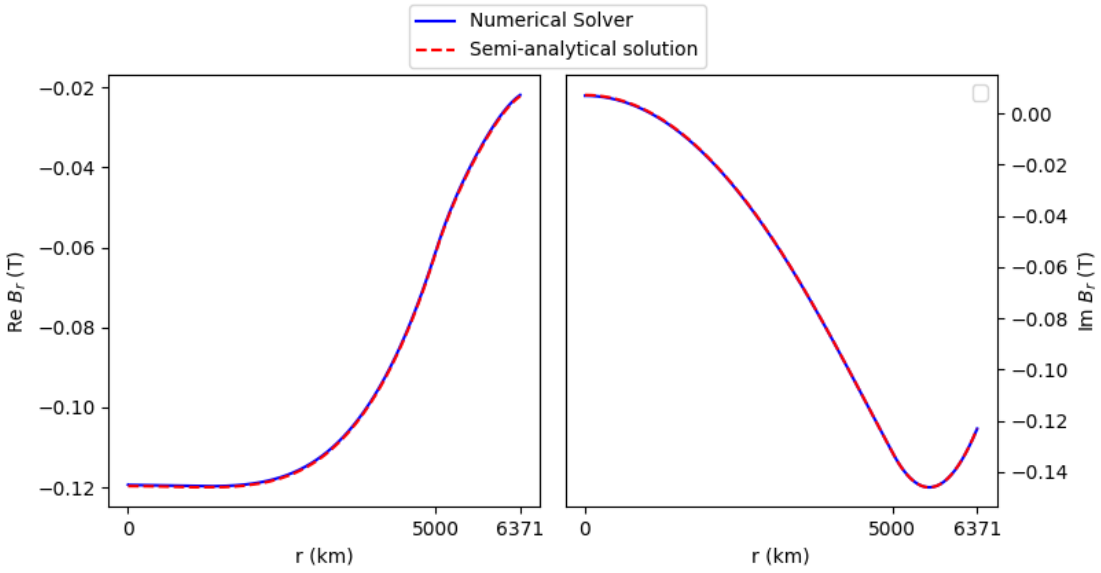


Figure 3.2: Radial depedence of the real and imaginary components $B_r$ at fixed colatitude $\vartheta = 140$ degrees.

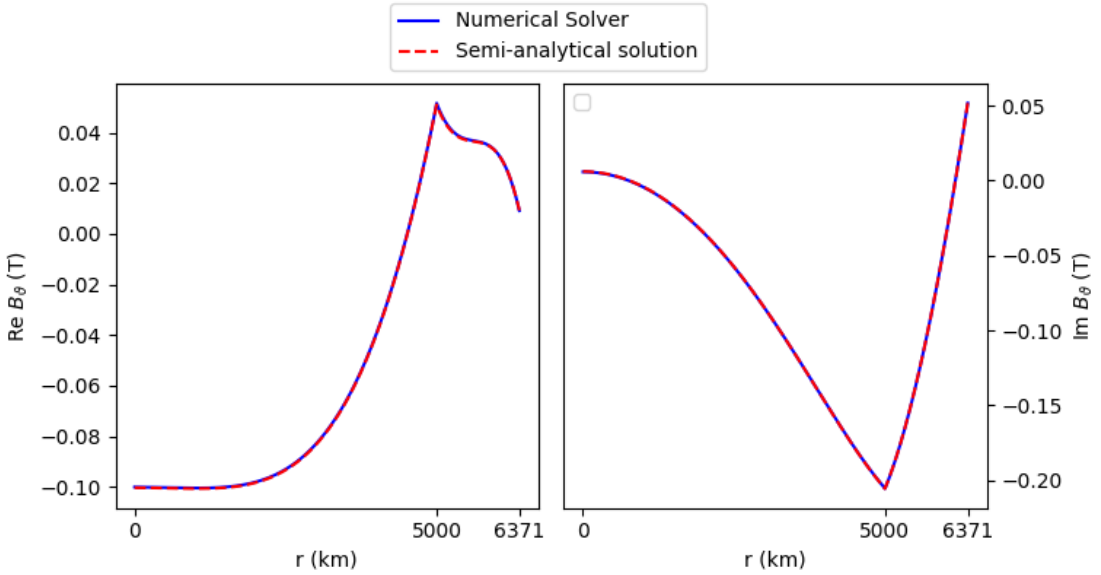


Figure 3.3: Radial depedence of the real and imaginary components $B_\vartheta$ at fixed colatitude $\vartheta = 140$ degrees.

# 4. Modelling setup

## 4.1 Inner structure of Europa and conductivity profiles

We use a simplified model of Europa consisting of three spherical layers ordered from inside to the surface: silicate mantle, ocean layer and ice shell. An artistic depiction is shown in Figure 4.1, however note that our simplified model does not include the highly conductive metallic core. Its presence would lead to a steeper attenuation of the OIMF as $r \to 0$.

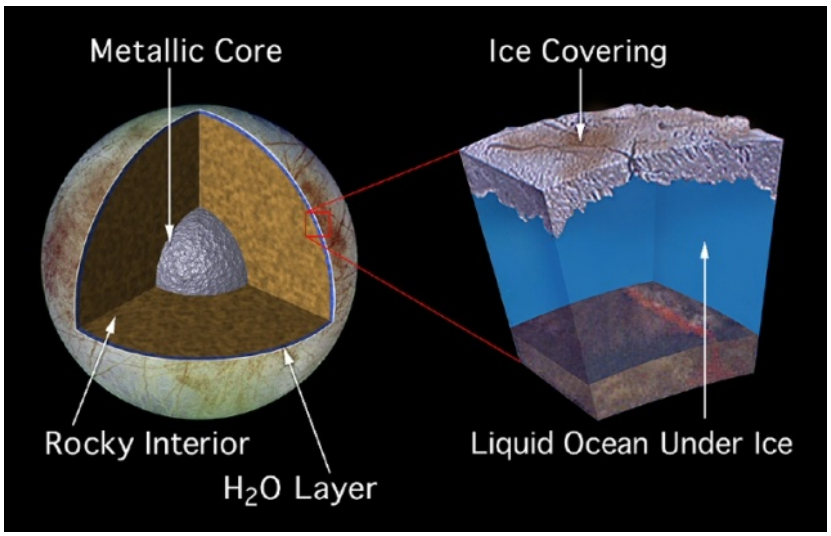


Figure 4.1: Artistic description of the internal structure of Europa. Modified from an original image by NASA (public domain). Source page: http://photojournal.jpl.nasa.gov/catalog/PIA01669.

The mantle of the Europa is made of the silicates, so we take the conductivity $\sigma_{mantle} = 10^{-4}$ S/m.

As discussed in (Vance et al. [2021]), the flux of oxygen generated on the surface of the ocean can create acidic conditions and lead to the presence of $MgSO_4$ in the subsurface ocean. Based on their previous work (Vance et al. [2018]), they assume $MgSO_4$ salinity of 10 $wt\%$. Alternatively, an Earth-like ocean composition is assumed with $NaCl$ salinity of 3.5165 $wt\%$, which we further call just seawater. In addition, they also tested models, where salinity is reduced by factor of 10. All relevant parameters of the four ocean types are described in Table 4.1. The thicknesses of the surface ice and subsurface ocean are also varied.

Ice is generally very bad conductor and its conductivity depends on presence of cracks filled with saline fluid, hence we explore a rather wide range of conductivities $\sigma_{ice} \approx 10^{-9} - 10^{-4}$ S/m.

| Model | | $D_o$ (km) | $D_i$ (km) | $\bar{\sigma}$ (S/m) | $\sigma_{top}$ (S/m) |
|---|---|---|---|---|---|
| Aa | $MgSO_4$ 1 $wt\%$ | 117 | 5 | 0.4533 | 0.4107 |
| Ab | $MgSO_4$ 1 $wt\%$ | 91 | 30 | 0.4132 | 0.3847 |
| Ba | $MgSO_4$ 10 $wt\%$ | 124 | 5 | 3.7646 | 3.3197 |
| Bb | $MgSO_4$ 10 $wt\%$ | 96 | 30 | 3.3661 | 3.0763 |
| Ca | Seawater 0.35165 $wt\%$ | 117 | 5 | 0.3855 | 0.3415 |
| Cb | Seawater 0.35165 $wt\%$ | 91 | 30 | 0.3651 | 0.3339 |
| Da | Seawater 3.5165 $wt\%$ | 119 | 5 | 3.0760 | 2.7347 |
| Db | Seawater 3.5165 $wt\%$ | 91 | 30 | 2.8862 | 2.6476 |

Table 4.1: $D_o, D_i$ denote the thicknesses of ocean and ice layer, $\bar{\sigma}$ is the mean value of conductivity in the ocean, and $\sigma_{top}$ is the value of conductivity at the ice–ocean interface. Radial depedency of conducitivity profiles is plotted in Figure (4.2). These parameters are taken from (Vance et al. [2021], pages 9–10).

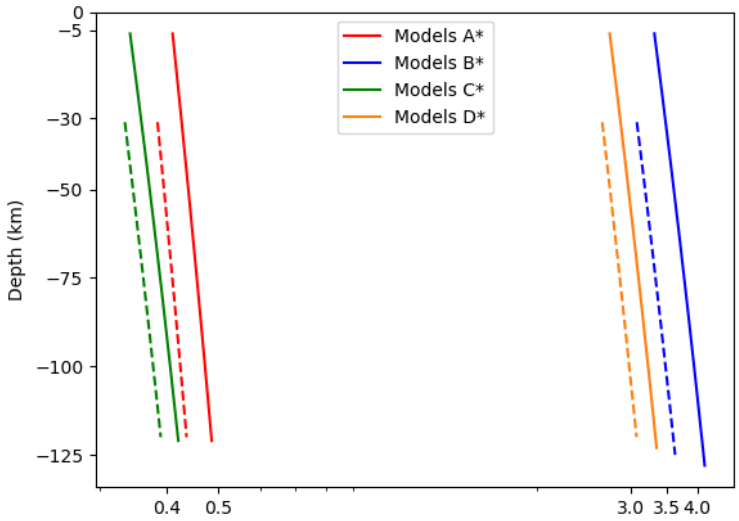


Figure 4.2: Depth dependent conductivity profiles in Europa ocean. The continuous and the dashed lines correspond respectively to $D_i = 5$ km (*a models) and to $D_i = 30$ km (*b models).

## 4.2 Jovian ambient magnetic field

In all models a homogeneous Jovian magnetic field is assumed, expressed in spherical coordinates as

$$\mathbf{B}_J(\vartheta) = -B_J(\cos(\vartheta), -\sin(\vartheta), 0), \tag{4.1}$$

which passes Europa in the direction of axis from north to south pole. Constant $B_J$ represents magnitude of Jovian magnetic field near Europa and its value is calculated as

$$B_J = B_R \left(\frac{R_J}{R_o}\right)^3 \approx 5.046 \cdot 10^2 \text{ nT}.$$

$B_R = 4.17 \cdot 10^5$ nT is magnitude of field at Jupiter's equator, $R_J = 7.1492 \cdot 10^7$ m is radius of the Jupiter and $R_o = 6.709 \cdot 10^8$ m is the mean orbital radius of

Europa.

By neglecting the movements of Europa in the Jovian magnetic field, the EMI equation (1.6) for Europa is simplified to

$$\mu_0 \frac{\partial \mathbf{B}}{\partial t} + \nabla \times \left( \frac{1}{\sigma} \nabla \times \mathbf{B} \right) = \mu_0 \nabla \times \mathbf{L}. \tag{4.2}$$

## 4.3 Simplified velocity models

Three simple analytical velocity models are created. We describe these models with their corresponding imposed electrical fields $\mathbf{L}$ in subsections (4.3.1–4.3.3).

All models have velocities, which satisfy the non–divergence property

$$\nabla \cdot \mathbf{u} = \mathbf{0}.$$

For simplicity, we assume stationary velocity fields in the presented models, hence we aim to integrate the EMI equation (1.6), until it reaches a stationary solution. From the estimation of Europa's ocean flow (Vance et al. [2021], page 19), conditions on velocities are placed

$$|u_r| \leq 0.07 \text{ m/s}, \qquad |u_\vartheta| \leq 0.3 \text{ m/s}, \qquad |u_\varphi| \leq 3 \text{ m/s}. \tag{4.3}$$

### 4.3.1 Model 1

We assume axisymmetric zonal flow

$$\mathbf{u} = \begin{pmatrix} 0 \\ 0 \\ C_u \sin(\vartheta) \end{pmatrix}, \tag{4.4}$$

where $C_u = 3$ m/s in order to satisfy (4.3). A cross-section of the flow is displayed in Figure 4.3. Then

$$\mathbf{L} = \mathbf{u} \times \mathbf{B}_J = -B_J C_u \begin{pmatrix} \sin^2(\vartheta) \\ \cos(\vartheta)\sin(\vartheta) \\ 0 \end{pmatrix}. \tag{4.5}$$

By using definition of spherical harmonic vectors, a following expansion can be made,

$$\mathbf{L} = L_{00}^{(-1)} \mathbf{S}_{00}^{(-1)} + L_{20}^{(-1)} \mathbf{S}_{20}^{(-1)} + L_{20}^{(1)} \mathbf{S}_{20}^{(1)}. \tag{4.6}$$

Only the coefficients $L_{20}^{(-1)}$ and $L_{20}^{(1)}$

$$L_{20}^{(-1)} = \frac{2}{3}\sqrt{\frac{4\pi}{5}} B_J C_u, \tag{4.7}$$

$$L_{20}^{(1)} = -\frac{1}{3}\sqrt{\frac{4\pi}{5}} B_J C_u, \tag{4.8}$$

are used in the computation. The coefficient $L_{00}^{(-1)}$ is omitted due to the definition of spherical harmonic expansion in subsection 1.2.1.

As the imposed electric field $\mathbf{L}$ is purely poloidal, its rotation is toroidal, and therefore the motionally induced magnetic field is fully described by a single toroidal term,

$$\mathbf{B} = B_{20}^{(0)} \mathbf{S}_{20}^{(0)}. \tag{4.9}$$

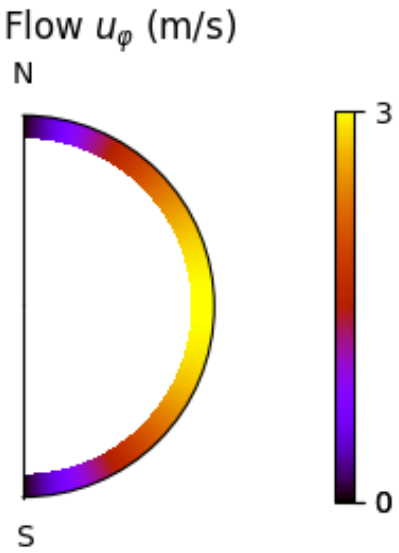


Figure 4.3: Model 1: Zonal velocity $u_\varphi$. In this case, there are only prograde flows.

### 4.3.2 Model 2

We assume velocity

$$\mathbf{u} = C_u \begin{pmatrix} u_1(r)\cos(\vartheta) \\ -\left(u_1(r) + u_2(r)\right)\sin(\vartheta) \\ 0 \end{pmatrix}, \tag{4.10}$$

where

$$u_1(r) = \sin\left(\pi \frac{r - r_1}{r_2 - r_1}\right), \tag{4.11}$$

$$u_2(r) = \frac{\pi r}{2(r_2 - r_1)} \cos\left(\pi \frac{r - r_1}{r_2 - r_1}\right), \tag{4.12}$$

and again, enforcing (4.3) only for $u_r$, so $C_u = 0.07$ m/s. Note that this flow satisfies the impermeable boundary conditions on both ocean interfaces. As seen in the cross-section in Figure 4.4, the flow pattern consists of a single convection cell with an upwelling located at the north pole, and a downwelling at the south pole. Then, the imposed electric field $\mathbf{L}$ is expressed as

$$\mathbf{L} = \mathbf{u} \times \mathbf{B}_J = -B_J C_u \begin{pmatrix} 0 \\ 0 \\ u_2(r)\cos(\vartheta)\sin(\vartheta) \end{pmatrix} = L_{20}^{(0)} \mathbf{S}_{20}^{(0)}, \tag{4.13}$$

$$L_{20}^{(0)} = \frac{1}{3}\sqrt{\frac{4\pi}{5}} B_J C_u u_2(r). \tag{4.14}$$

As the imposed electric field $\mathbf{L}$ is purely toroidal, its rotation is poloidal, and therefore the motionally induced magnetic field is fully described by two poloidal terms,

$$\mathbf{B} = B_{20}^{(-1)} \mathbf{S}_{20}^{(-1)} + B_{20}^{(1)} \mathbf{S}_{20}^{(1)}. \tag{4.15}$$

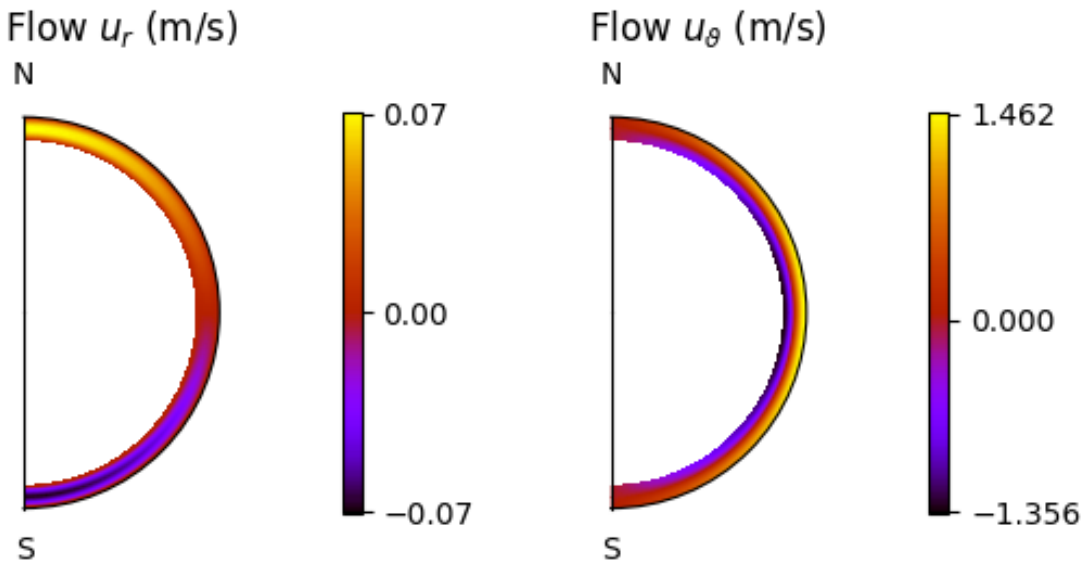


Figure 4.4: Model 2: Radial velocity $u_r$ and meridional velocity $u_\vartheta$. For $u_r$, positive (negative) values denote upwelling (downwelling) flows, and for $u_\vartheta$, positive (negative) values denote flows coming from the north pole (toward the north pole).

### 4.3.3 Model 3

We assume velocity

$$\mathbf{u} = C_u \begin{pmatrix} -u_1(r)(6\cos^2(\vartheta) - 2) \\ (2u_1(r) + u_2(r))\sin(2\vartheta) \\ 0 \end{pmatrix}, \tag{4.16}$$

where

$$u_1(r) = \sin\left(\pi \frac{r - r_1}{r_2 - r_1}\right), \tag{4.17}$$

$$u_2(r) = \frac{\pi r}{(r_2 - r_1)} \cos\left(\pi \frac{r - r_1}{r_2 - r_1}\right), \tag{4.18}$$

and again, we use (4.3) to constrain the flow amplitude of $u_r$, so $C_u = 7/400$ m/s. As shown in Figure 4.5, there is an upwelling located at the equator, with two convection cells carrying the water respectively to the northern and southern poles, where it descends to the ocean bottom. The imposed electric field $\mathbf{L}$ is expressed as

$$\begin{aligned} \mathbf{L} = \mathbf{u} \times \mathbf{B}_J &= -2B_J C_u \begin{pmatrix} 0 \\ 0 \\ ((u_1(r) - u_2(r))\cos^2(\vartheta) - u_1(r))\sin(\vartheta) \end{pmatrix} = \\ &= L_{10}^{(0)} \mathbf{S}_{10}^{(0)} + L_{30}^{(0)} \mathbf{S}_{30}^{(0)}, \end{aligned} \tag{4.19}$$

$$L_{10}^{(0)} = -\frac{2}{5}\sqrt{\frac{4\pi}{3}} B_J C_u (4u_1(r) + u_2(r)), \tag{4.20}$$

$$L_{30}^{(0)} = \frac{4}{15}\sqrt{\frac{4\pi}{7}} B_J C_u (u_1(r) - u_2(r)). \tag{4.21}$$

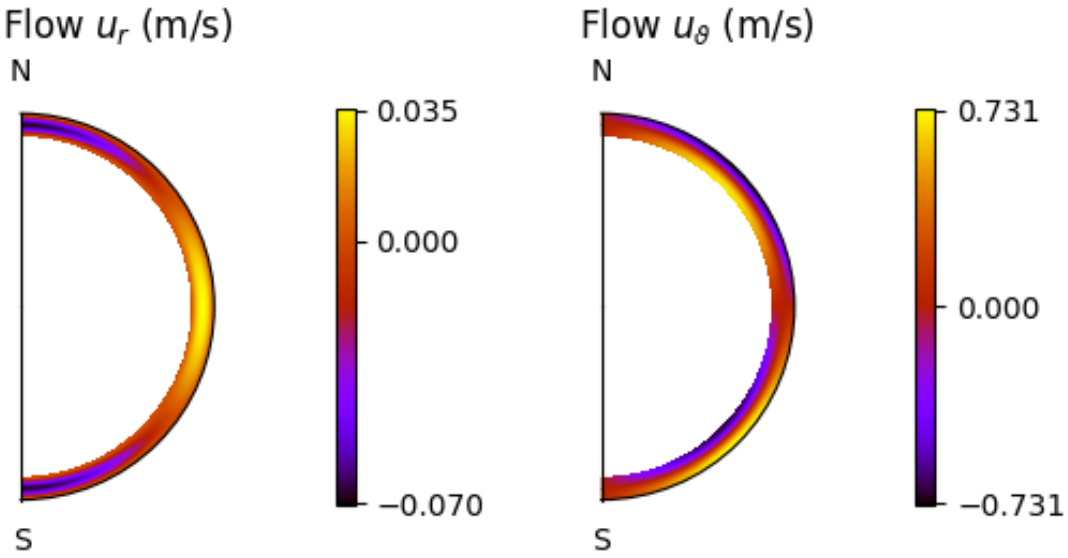


Figure 4.5: Model 3: Radial velocity $u_r$ and meridional velocity $u_\vartheta$.

As the imposed electric field $\mathbf{L}$ is purely toroidal, its rotation is poloidal, and therefore the motionally induced magnetic field is fully described by four poloidal terms,

$$\mathbf{B} = B_{10}^{(-1)}\mathbf{S}_{10}^{(-1)} + B_{10}^{(1)}\mathbf{S}_{10}^{(1)} + B_{30}^{(-1)}\mathbf{S}_{30}^{(-1)} + B_{30}^{(1)}\mathbf{S}_{30}^{(1)}. \tag{4.22}$$

# 5. Results

## 5.1 Model 1

In Model 1, there is no big differences between the OIMFs calculated for different ice conductivities, so I only show results for $\sigma_{ice} = 10^{-9}$ S/m. Figure 5.1 shows the radial profiles of the zonal magnetic field along fixed colatitude of 45 degrees. For all conductivity models the magnetic field is contained in the ocean layer. It quickly diffuses both downwards to the sillicate mantle and upwards to the ice shell. As demonstrated in the cross-section plots in Figures 5.2a and 5.2b, the field has opposite signs in the northern and southern hemisphere. On the ice-atmosphere boundary, it is exactly zero as required by the boundary condition.

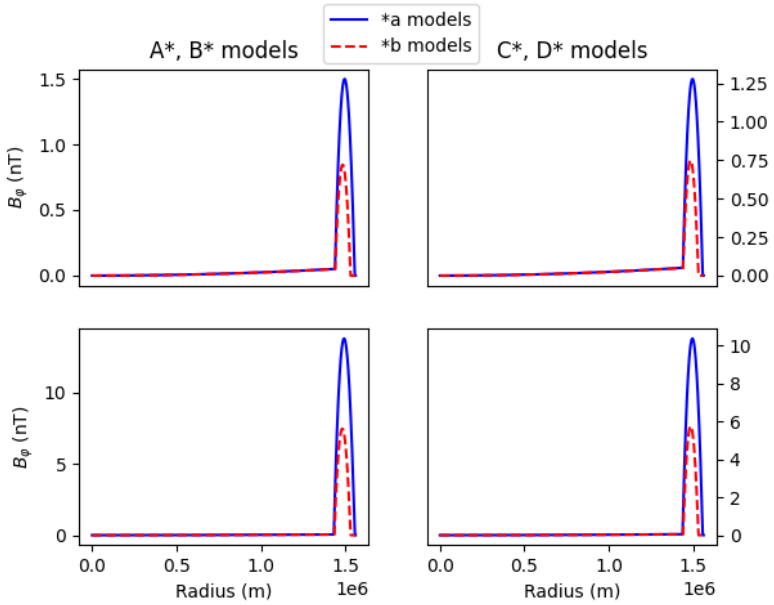


Figure 5.1: Model 1: Component $B_\varphi$, at colatitude $\vartheta = 45$ degrees. In first row are oceans with lower salinities in second row are oceans with higher salinities.

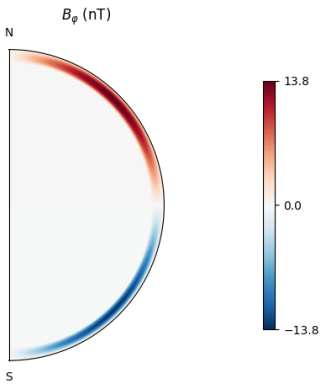


(a) Model 1: Cross-section of the zonal magnetic field $B_\varphi$, conductivity Ba.

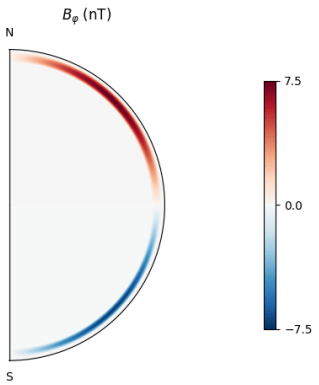


(b) Model 1: Cross-section of the zonal magnetic field $B_\varphi$, conductivity Bb.

## 5.2 Model 2

### 5.2.1 Low-salinity models

In case of Model 2 and low-salinity profiles A* and C*, we show in Figure 5.3 the radial profiles of $B_r$ and $B_\vartheta$ for ice layer conductivities $\sigma_{ice} = 10^{-9} - 10^{-8}$ S/m. The solution depends both on the ice conductivity and thickness. For higher ice conductivities, the differences between the solutions are reduced. In Figure 5.4 we show the quadrupolar spatial structure of the OIMF. In general, the OIMFs generated for low salinity profiles have small amplitudes on the surface and would be difficult to observe.

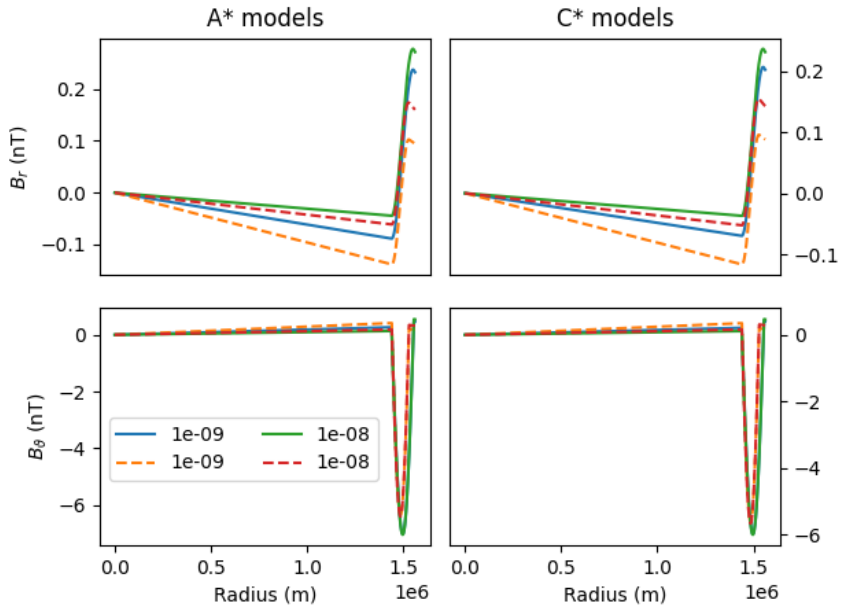


Figure 5.3: Model 2: Components $B_r$ and $B_\vartheta$, at colatitude $\vartheta = 45$ degrees. Lower salinities, continous line for 5 km ice thickness and dashed line for 30 km ice thickness. Colour markings correspond to the ice layer conductivity.

### 5.2.2 High-salinity models

Figure 5.5 shows the OIMF profiles for the high-salinity models B* and D*. Here the OIMFs are systematically stronger than in the low-salinity cases. The quadrupolar structure is preserved as demonstrated in Figure 5.6, where we show the run with the highest amplitudes.

## 5.3 Model 3

The effects of the ocean salinities and ice conductivities and thicknesses in case of Model 3 are similar to the case of Model 2. We summarize the radial profiles for the low-salinity cases in Figure 5.7, and for the high-salinity cases in Figure 5.8. In Figure 5.9 we show the results with the largest amplitude of the radial OIMF component, which was obtained for the ice thickness of 5 km, and the ice

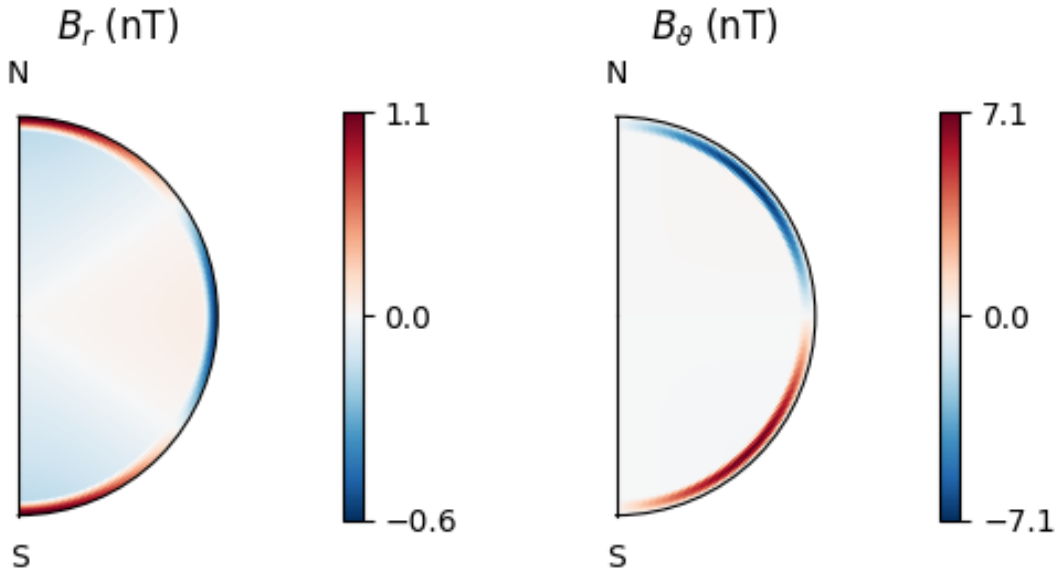


Figure 5.4: Model 2: Cross-sections of the OIMF, conductivity model Aa, $\sigma_{ice} = 10^{-8}$ S/m.

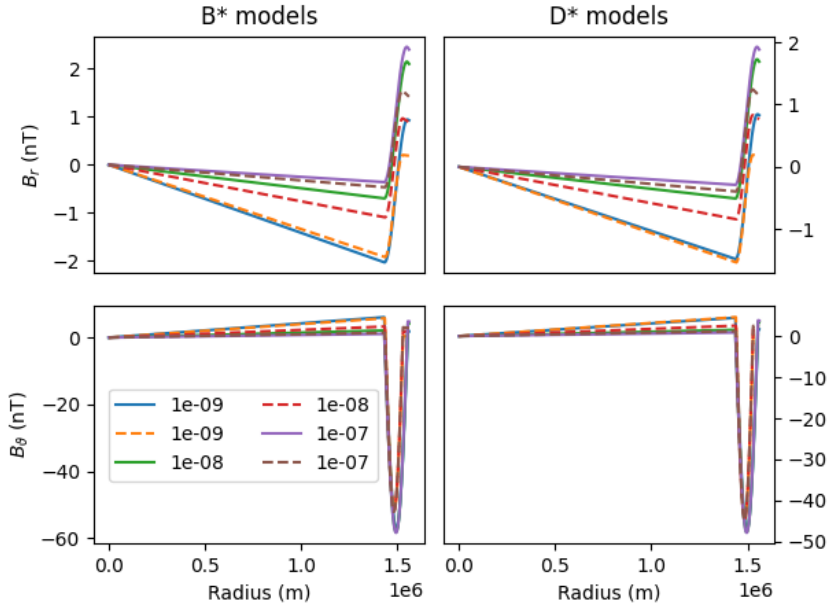


Figure 5.5: Model 2: Components $B_r$ and $B_\vartheta$, at colatitude $\vartheta = 45$ degrees. Higher salinities, continous line for 5 km ice thickness and dashed line for 30 km ice thickness. Colour markings correspond to the ice layer conductivity.

conductivity of $10^{-9}$ S/m. However, note that the OIMF now displays a spatial structure, which is a combination of dipole and octupole, as demonstrated by the cross-sections in Figure 5.9.

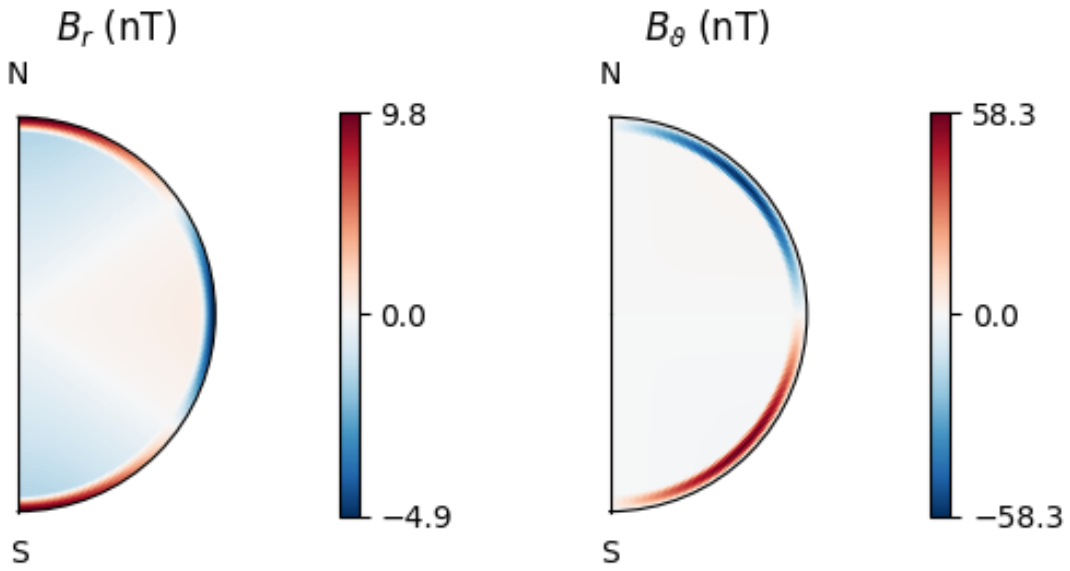


Figure 5.6: Model 2: Cross-sections of the OIMF, conductivity model Ba, $\sigma_{ice} = 10^{-7}$ S/m.

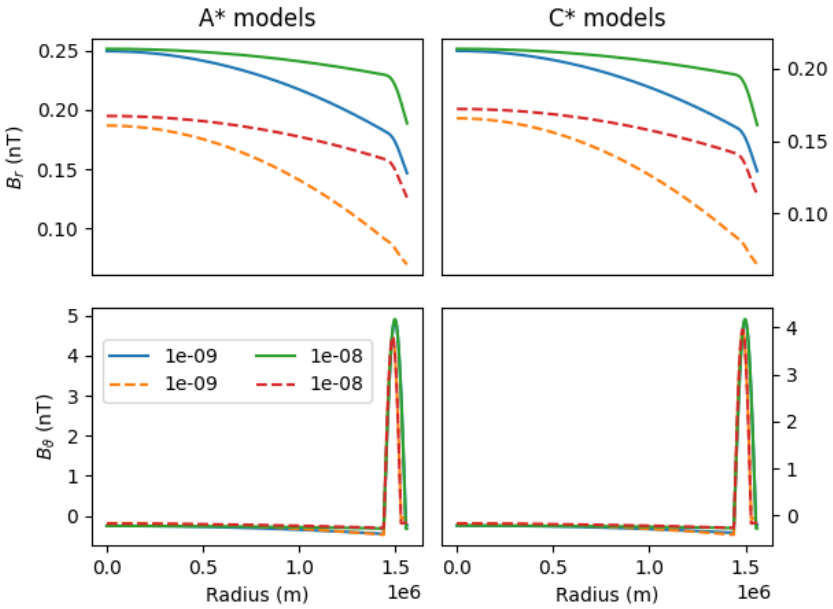


Figure 5.7: Model 3: Components $B_r$ and $B_\vartheta$, at colatitude $\vartheta = 45$ degrees. Lower salinities, continous line for 5 km ice thickness and dashed line for 30 km ice thickness. Colour markings correspond to the ice layer conductivity.

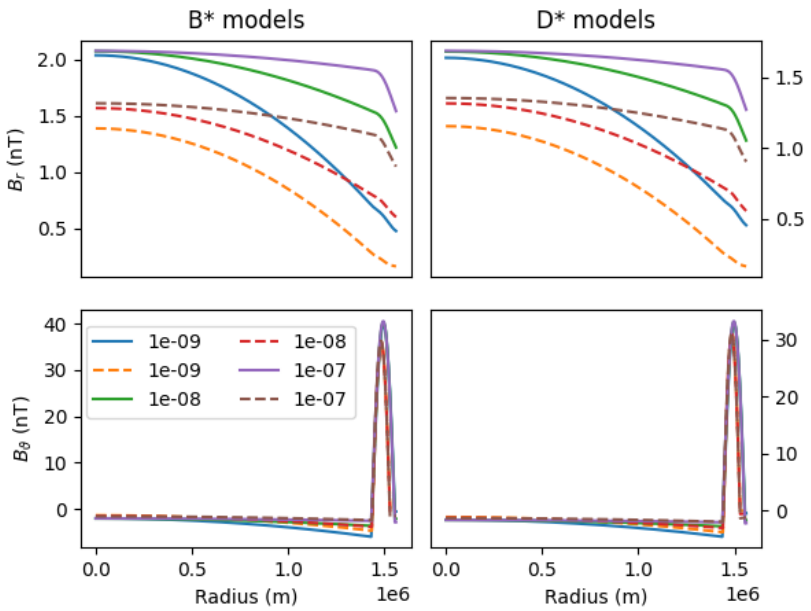


Figure 5.8: Model 3: Components $B_r$ and $B_\vartheta$, at colatitude $\vartheta = 45$ degrees. Higher salinities, continous line for 5 km ice thickness and dashed line for 30 km ice thickness. Colour markings correspond to the ice layer conductivity.

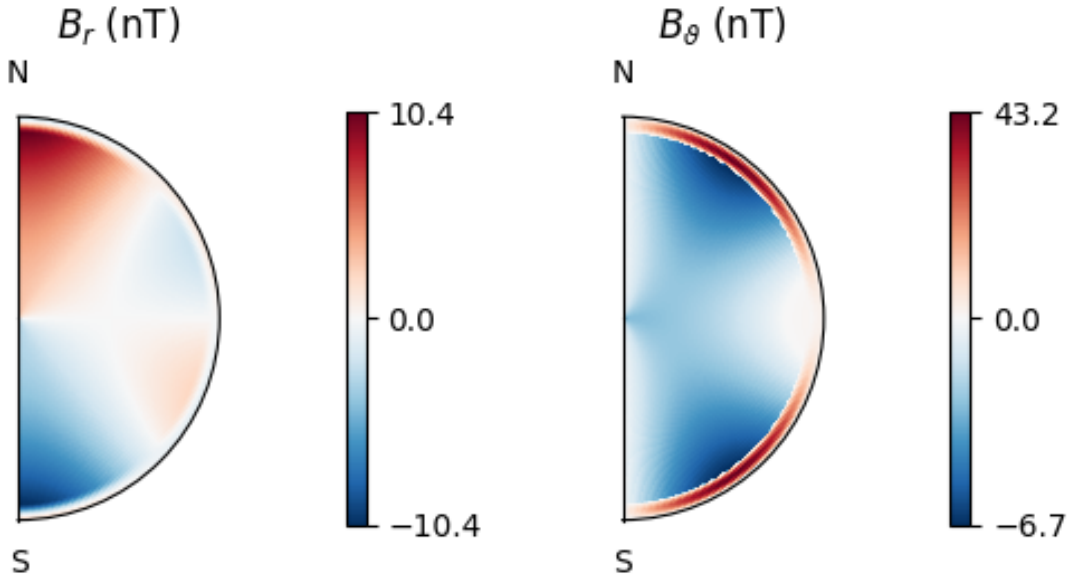


Figure 5.9: Model 3: Cross-sections of the OIMF, conductivity model Ba, $\sigma_{ice} = 10^{-9}$ S/m.

# Conclusion

The calculations presented in this thesis demonstrate, that the conductivity of the ice layer has noticeable effect on the induced fields. Strongest signals are achieved in cases with higher salinity of ocean, less conductive ice and thinner ice shell.

By its definition, the toroidal part of $\mathbf{B}$ disappears on the conductor-insulator interface, hence the toroidal OIMF is directly observable neither on Europa's surface (by a future lander), nor by near flybys (JUICE and Europa Clipper). A submarine mission to the Europa's ocean, contemplated by space agencies, but probably beyond the reach of present technology, would be needed for its direct observations.

However, the poloidal part of the field can be measured by space missions Europa Clipper and JUICE. From our estimates, the signal on the ice–atmosphere boundary is in the range $\approx 10^{-1}$ nT to $\approx 10^{2}$ nT, thus confirming the back-of-the-envelope estimates of (Vance et al. [2021]). Strength of the signal is highly dependent on ocean and ice conductivities, thickness of ice shell and ocean velocities. We can also assume, that Jovian magnetic field will have effect.

In this thesis, a strongly simplified model of the ambient Jovian magnetic field $\mathbf{B}_J$ is used. It only represents the amplitude scaled to distance of Europa. For future tests, models of the Jovian magnetic field from (Connerney et al. [2022]) should be employed. Also, we neglect its time variations and changes of orientation in the Europa's internal reference frame stemming from the movements of Europa along its orbit.

Finally, the velocity models employed in this work represent only crude simplifications of possible flow patterns in the Europa's ocean (Soderlund et al. [2014]). There are also plans to exploit the ocean flow models based on the work of (Kvorka and Čadek [2022]) for Europa.

# Bibliography

George Backus. Poloidal and toroidal fields in geomagnetic field modeling. *Reviews of geophysics (1985)*, 24(1):75–109, 1986. ISSN 8755-1209.

Michel Blanc, Olga Prieto-Ballesteros, Nicolas André, Javier Gomez-Elvira, Geraint Jones, Veerle Sterken, William Desprats, Leonid I. Gurvits, Krishan Khurana, Georges Balmino, Aljona Blöcker, Renaud Broquet, Emma Bunce, Cyril Cavel, Gaël Choblet, Geoffrey Colins, Marcello Coradini, John Cooper, Dominic Dirkx, Dominique Fontaine, Philippe Garnier, David Gaudin, Paul Hartogh, Hauke Hussmann, Antonio Genova, Luciano Iess, Adrian Jäggi, Sascha Kempf, Norbert Krupp, Luisa Lara, Jérémie Lasue, Valéry Lainey, François Leblanc, Jean-Pierre Lebreton, Andrea Longobardo, Ralph Lorenz, Philippe Martins, Zita Martins, Jean-Charles Marty, Adam Masters, David Mimoun, Ernesto Palumba, Victor Parro, Pascal Regnier, Joachim Saur, Adriaan Schutte, Edward C. Sittler, Tilman Spohn, Ralf Srama, Katrin Stephan, Károly Szegő, Federico Tosi, Steve Vance, Roland Wagner, Tim Van Hoolst, Martin Volwerk, Jan-Erik Wahlund, Frances Westall, and Peter Wurz. Joint europa mission (jem): a multi-scale study of europa to characterize its habitability and search for extant life. *Planetary and space science*, 193:104960–, 2020. ISSN 0032-0633.

J. E. P. Connerney, S. Timmins, R. J. Oliversen, J. R. Espley, J. L. Joergensen, S. Kotsiaros, P. S. Joergensen, J. M. G. Merayo, M. Herceg, J. Bloxham, K. M. Moore, A. Mura, A. Moirano, S. J. Bolton, and S. M. Levin. A new model of jupiter's magnetic field at the completion of juno's prime mission. *Journal of geophysical research. Planets*, 127(2), 2022. ISSN 2169-9097.

Alexander V. Grayver, Federico D. Munch, Alexei V. Kuvshinov, Amir Khan, Terence J. Sabaka, and Lars Tøffner-Clausen. Joint inversion of satellite-detected tidal and magnetospheric signals constrains electrical conductivity and water content of the upper mantle and transition zone. 44:6074–6081, 2017.

K. K Khurana, M. G Kivelson, D. J Stevenson, G Schubert, C. T Russell, R. J Walker, and C Polanskey. Induced magnetic fields as evidence for subsurface oceans in europa and callisto. *Nature (London)*, 395(6704):777–780, 1998. ISSN 0028-0836.

Jakub Kvorka and Ondřej Čadek. A numerical model of convective heat transfer in titan's subsurface ocean. *Icarus (New York, N.Y. 1962)*, 376:114853–, 2022. ISSN 0019-1035.

K M Soderlund, B E Schmidt, J Wicht, and D D Blankenship. Ocean-driven heating of europa's icy shell at low latitudes. *Nature geoscience*, 7(1):16–19, 2014. ISSN 1752-0894.

S. D. Vance, M. J. Styczinski, B. G. Bills, C. J. Cochrane, K. M. Soderlund, N. Gómez-Pérez, and C. Paty. Magnetic induction responses of jupiter's ocean

moons including effects from adiabatic convection. *Journal of geophysical research. Planets*, 126(2), 2021. ISSN 2169-9097.

Steven D. Vance, Mark P. Panning, Simon C. Staehler, Fabio Cammarano, Bruce G. Bills, Gabriel Tobie, Shunichi Kamata, Sharon Kedar, Christophe Sotin, William T. Pike, Ralph D. Lorenz, Hsin-Hua Huang, Jennifer M. Jackson, and Bruce Banerdt. Geophysical investigations of habitability in ice-covered ocean worlds. *Journal of geophysical research. Planets*, 123(1):180–205, 2018. ISSN 2169-9097.

D. A. (Dmitrii Aleksandrovich) Varshalovich. *Quantum theory of angular momentum : Irreducible tensors, spherical harmonics, vector coupling coefficients 3 nj symbols*. World Scientific Pub., Singapore ;, 1989. ISBN 981-4415-49-9.

J. Velímský and Z. Martinec. Time-domain, spherical harmonic-finite element approach to transient three-dimensional geomagnetic induction in a spherical heterogeneous Earth. 160:81–101, 2005.

J. Velímský, N. R. Schnepf, M. C. Nair, and N. P. Thomas. Can seafloor voltage cables be used to study large-scale circulation? an investigation in the pacific ocean. *Ocean Science*, 17(1):383–392, 2021. doi: 10.5194/os-17-383-2021. URL `https://os.copernicus.org/articles/17/383/2021/`.

# List of Figures

# List of Tables

# A. Appendix

## A.1 Poloidal–toroidal decomposition

Using a poloidal–toroidal decomposition (Backus [1986]), which is a restricted form of the Helmholtz decomposition, a non–divergent 3–D vector field $\mathbf{f}$ can be decomposed into a toroidal field $\mathbf{f}_T$ and a poloidal field $\mathbf{f}_P$,

$$\mathbf{f} = \mathbf{f}_T + \mathbf{f}_P. \tag{A.1}$$

The toroidal field is obtained from a scalar field $\Psi(\mathbf{r})$,

$$\mathbf{f}_T = \nabla \times (\mathbf{r}\Psi(\mathbf{r})), \tag{A.2}$$

and the poloidal field is obtained from another scalar field $\Phi(\mathbf{r})$,

$$\mathbf{f}_P = \nabla \times (\nabla \times (\mathbf{r}\Phi(\mathbf{r}))). \tag{A.3}$$

## A.2 Spherical harmonic functions

In this appendix, the real, fully normalized spherical harmonic scalar and vector functions are defined, analogous to their complex counterparts in (Varshalovich [1989]).

The scalar spherical harmonic function is defined as

$$Y_{jm}(\Omega) = \begin{cases} (-1)^m \sqrt{2} \sqrt{\frac{2j+1}{4\pi} \frac{(j-m)!)}{(j+m)!)}} P_j^m(\cos\vartheta) \cos(m\varphi) & , \ m > 0 \\ \sqrt{\frac{2j+1}{4\pi}} P_j^0(\cos\vartheta) & , \ m = 0 \\ (-1)^m \sqrt{2} \sqrt{\frac{2j+1}{4\pi} \frac{(j-|m|)!)}{(j+|m|)!)}} P_j^{|m|}(\cos\vartheta) \sin(|m|\varphi) & , \ m < 0 \end{cases} \tag{A.4}$$

where $j$ is the degree, $m$ is the order, $|m| \leq j$, $\Omega = (\vartheta, \varphi)$ and $P_j^m(\cos\vartheta)$ are the associated Legendre polynomials

$$P_j^m(\cos\vartheta) = (-\sin\vartheta)^m \frac{d^m}{(d\cos\vartheta)^m} P_j(\cos\vartheta). \tag{A.5}$$

The $Y_{jm}(\Omega)$ functions are orthonormal on a unit sphere

$$\int_\Omega Y_{jm}(\Omega) Y_{j'm'}(\Omega) d\Omega = \delta_{jj'}\delta_{mm'}. \tag{A.6}$$

With the radial unit vector $\mathbf{e}_r$ and the angular gradient operator $\nabla_\Omega$, the following vectors are constructed,

$$\mathbf{S}_{jm}^{(-1)}(\Omega) = Y_{jm}(\Omega)\mathbf{e}_r, \tag{A.7}$$

$$\mathbf{S}_{jm}^{(0)}(\Omega) = \mathbf{e}_r \times \nabla_\Omega Y_{jm}(\Omega), \tag{A.8}$$

$$\mathbf{S}_{jm}^{(1)}(\Omega) = \nabla_\Omega Y_{jm}(\Omega). \tag{A.9}$$

These, respectively, describe the vertical poloidal–scaloidal, the toroidal and the horizontal poloidal–scaloidal components of a vector field and satisfy relations

$$\mathbf{e}_r \times \mathbf{S}_{jm}^{(0)} = -\mathbf{S}_{jm}^{(1)}, \tag{A.10}$$

$$\mathbf{e}_r \times \mathbf{S}_{jm}^{(1)} = \mathbf{S}_{jm}^{(0)}, \tag{A.11}$$

$$\mathbf{e}_r \times \mathbf{S}_{jm}^{(-1)} = \mathbf{0}. \tag{A.12}$$

These vectors are orthogonal on a unit sphere,

$$\int_\Omega \mathbf{S}_{jm}^{(\lambda)}(\Omega) \cdot \mathbf{S}_{j'm'}^{(\lambda')}(\Omega) d\Omega = \delta_{jj'}\delta_{mm'}\delta_{\lambda\lambda'}N_{j\lambda}, \tag{A.13}$$

where $N_{j\lambda} = \delta_{-1\lambda} + j(j+1)(1-\delta_{-1\lambda})$.

The spherical harmonic functions interact with vector operators. For an arbitrary, sufficiently smooth function $f(r)$ holds:

**Gradient operator**:

$$\nabla \left[f(r)Y_{jm}(\Omega)\right] = \frac{df(r)}{dr}\mathbf{S}_{jm}^{(-1)} + \frac{f(r)}{r}\mathbf{S}_{jm}^{(1)}. \tag{A.14}$$

**Divergence operator**:

$$\nabla \cdot \left[f(r)\mathbf{S}_{jm}^{(-1)}(\Omega)\right] = \left(\frac{d}{dr} + \frac{2}{r}\right) f(r)Y_{jm}, \tag{A.15}$$

$$\nabla \cdot \left[f(r)\mathbf{S}_{jm}^{(0)}(\Omega)\right] = 0, \tag{A.16}$$

$$\nabla \cdot \left[f(r)\mathbf{S}_{jm}^{(1)}(\Omega)\right] = -j(j+1)\frac{f(r)}{r}Y_{jm}. \tag{A.17}$$

**Rotation operator**:

$$\nabla \times \left[f(r)\mathbf{S}_{jm}^{(-1)}(\Omega)\right] = -\frac{f(r)}{r}\mathbf{S}_{jm}^{(0)}, \tag{A.18}$$

$$\nabla \times \left[f(r)\mathbf{S}_{jm}^{(0)}(\Omega)\right] = -j(j+1)\frac{f(r)}{r}\mathbf{S}_{jm}^{(-1)} - \left(\frac{d}{dr} + \frac{2}{r}\right) f(r)\mathbf{S}_{jm}^{(1)}, \tag{A.19}$$

$$\nabla \times \left[f(r)\mathbf{S}_{jm}^{(1)}(\Omega)\right] = \left(\frac{d}{dr} + \frac{2}{r}\right) f(r)\mathbf{S}_{jm}^{(0)}. \tag{A.20}$$

## A.3 1-D finite elements

Parameterization of radial component is done by 1-D finite elements. First, an arbitrary discretization of radial coordinate is made, $0 = r_1 < r_2 < \ldots < r_{k_{max}} < r_{k_{max}+1} = R_E$. Second, the piecewise linear finite element is defined as

$$\psi_k(r) = \begin{cases} \frac{r-r_{k-1}}{r_k-r_{k-1}} & r \in (r_{k-1}, r_k), \\ \frac{r_{k+1}-r}{r_{k+1}-r_k} & r \in (r_k, r_{k+1}), \\ 0 & r \notin (r_{k-1}, r_{k+1}). \end{cases} \tag{A.21}$$

For piecewise constant functions, we define

$$\xi_k(r) = \begin{cases} 1 & r \in (r_k, r_{k+1}), \\ 0 & r \notin (r_k, r_{k+1}). \end{cases} \tag{A.22}$$

## A.4 Integrals of finite-element products

$$I_{kk'} = \int_0^a r^2 \Psi_k \Psi_{k'} dr,$$

$$K^{(1)}_{kk'} = \int_0^a \frac{1}{\sigma_k} \Psi_k \Psi_{k'} dr, \qquad K^{(2)}_{kk'} = \int_0^a \frac{1}{\sigma_k} \chi^{(1)}_k \chi^{(1)}_{k'} dr,$$

$$K^{(3)}_{kk'} = \int_0^a \frac{1}{\sigma_k} \chi^{(1)}_k \Psi_{k'} dr, \qquad K^{(4)}_{kk'} = \int_0^a \frac{1}{\sigma_k} \Psi_k \chi^{(1)}_{k'} dr$$

$$\Theta^{(1)}_{kk'} = \int_0^a r\xi_k \Psi_{k'} dr, \qquad \Theta^{(2)}_{kk'} = \int_0^a r\xi_{k'} \Psi_k dr,$$

$$\Theta^{(3)}_{kk'} = \int_0^a r\xi_k \chi^{(1)}_{k'} dr, \qquad \Theta^{(4)}_{kk'} = \int_0^a r\xi_{k'} \chi^{(1)}_k dr,$$

$$\Theta^{(5)}_{kk'} = \int_0^a r\xi_k \chi^{(2)}_{k'} dr, \qquad \Theta^{(6)}_{kk'} = \int_0^a r\xi_{k'} \chi^{(2)}_k dr,$$

where $\chi^{(1)}_k(r)$ is defined as

$$\chi^{(1)}_k(r) = r\left(\frac{d}{dr} + \frac{1}{r}\right)\psi_k = \begin{cases} \frac{2r - r_{k-1}}{r_k - r_{k-1}} & r \in (r_{k-1}, r_k), \\ \frac{r_{k+1} - 2r}{r_{k+1} - r_k} & r \in (r_k, r_{k+1}), \\ 0 & r \notin (r_{k-1}, r_{k+1}), \end{cases} \tag{A.23}$$

and $\chi^{(2)}_k(r)$ as

$$\chi^{(2)}_k(r) = r\left(\frac{d}{dr} + \frac{2}{r}\right)\psi_k = \begin{cases} \frac{3r - 2r_{k-1}}{r_k - r_{k-1}} & r \in (r_{k-1}, r_k), \\ \frac{2r_{k+1} - 3r}{r_{k+1} - r_k} & r \in (r_k, r_{k+1}), \\ 0 & r \notin (r_{k-1}, r_{k+1}). \end{cases} \tag{A.24}$$

If $|k - k'| > 1$, or $min(k, k') = 0$, or $max(k, k') = k_{max} + 2$, defined integrals are zero. From definitions (A.21), (A.22), (A.23) and (A.24), $h_k = r_{k+1} - r_k$ ,for $k' = k$ holds

$$I_{kk} = \int_{r_{k-1}}^{r_k} r^2 \Psi_k \Psi_k dr + \int_{r_k}^{r_{k+1}} r^2 \Psi_k \Psi_k dr,$$

$$\int_{r_{k-1}}^{r_k} r^2 \Psi_k \Psi_k dr = \frac{h_{k-1}}{30}(6r_k^2 + 3r_k r_{k-1} + r_{k-1}^2)$$

$$\int_{r_k}^{r_{k+1}} r^2 \Psi_k \Psi_k dr = \frac{h_k}{30}(r_{k+1}^2 + 3r_{k+1} r_k + 6r_k^2)$$

$$K^{(1)}_k = \int_{r_{k-1}}^{r_k} \frac{1}{\sigma_{k-1}} \Psi_k \Psi_k dr + \int_{r_k}^{r_{k+1}} \frac{1}{\sigma_k} \Psi_k \Psi_k dr,$$

$$\int_{r_{k-1}}^{r_k} \frac{1}{\sigma_{k-1}} \Psi_k \Psi_k dr = \frac{h_{k-1}}{3\sigma_{k-1}}$$

$$\int_{r_k}^{r_{k+1}} \frac{1}{\sigma_k} \Psi_k \Psi_k dr = \frac{h_k}{3\sigma_k}$$

$$K_k^{(2)} = \int_{r_{k-1}}^{r_k} \frac{1}{\sigma_{k-1}} \chi_k^{(1)} \chi_k^{(1)} dr + \int_{r_k}^{r_{k+1}} \frac{1}{\sigma_k} \chi_k^{(1)} \chi_k^{(1)} dr,$$

$$\int_{r_{k-1}}^{r_k} \frac{1}{\sigma_{k-1}} \chi_k^{(1)} \chi_k^{(1)} dr = \frac{1}{3h_{k-1}\sigma_{k-1}} (4r_k^2 - 2r_k r_{k-1} + r_{k-1}^2)$$

$$\int_{r_k}^{r_{k+1}} \frac{1}{\sigma_k} \chi_k^{(1)} \chi_k^{(1)} dr = \frac{1}{3h_k\sigma_k} (r_{k+1}^2 - 2r_{k+1}r_k + 4r_k^2)$$

$$K_k^{(3)} = K_k^{(4)} = \int_{r_{k-1}}^{r_k} \frac{1}{\sigma_{k-1}} \Psi_k \chi_k^{(1)} dr + \int_{r_k}^{r_{k+1}} \frac{1}{\sigma_k} \Psi_k \chi_k^{(1)} dr,$$

$$\int_{r_{k-1}}^{r_k} \frac{1}{\sigma_{k-1}} \Psi_k \chi_k^{(1)} dr = \frac{4r_k - r_{k-1}}{6\sigma_{k-1}}$$

$$\int_{r_k}^{r_{k+1}} \frac{1}{\sigma_k} \Psi_k \chi_k^{(1)} dr = \frac{r_{k+1} - 4r_k}{6\sigma_k}$$

$$\Theta_k^{(1)} = \Theta_k^{(2)} = \int_{r_k}^{r_{k+1}} r\xi_k \Psi_k dr = \frac{h_k}{6}(r_{k+1} + 2r_k)$$

$$\Theta_k^{(3)} = \Theta_k^{(4)} = \int_{r_k}^{r_{k+1}} r\xi_k \chi_k^{(1)} dr = -\frac{1}{6}(r_{k+1}^2 + r_{k+1}r_k + 4r_k^2)$$

$$\Theta_k^{(5)} = \Theta_k^{(6)} = \int_{r_k}^{r_{k+1}} r\xi_k \chi_k^{(2)} dr = -r_k^2$$

for $k = \min(k, k')$ holds

$$I_k = \int_{r_k}^{r_{k+1}} r^2 \Psi_k \Psi_{k+1} dr = \frac{h_k}{60}(3r_{k+1}^2 + 4r_{k+1}r_k + 3r_k^2)$$

$$K_k^{(1)} = \int_{r_k}^{r_{k+1}} \frac{1}{\sigma_k} \Psi_k \Psi_{k+1} dr = \frac{h_k}{6\sigma_k}$$

$$K_k^{(2)} = \int_{r_k}^{r_{k+1}} \frac{1}{\sigma_k} \chi_k^{(1)} \chi_{k+1}^{(1)} dr = -\frac{1}{3h_k\sigma_k}(r_{k+1}^2 + r_{k+1}r_k + r_k^2)$$

for $k' = k + 1$ holds

$$K_{kk+1}^{(3)} = \int_{r_k}^{r_{k+1}} \frac{1}{\sigma_k} \Psi_{k+1} \chi_k^{(1)} dr = -\frac{r_{k+1} + 2r_k}{6\sigma_k}$$

$$K_{kk+1}^{(4)} = \int_{r_k}^{r_{k+1}} \frac{1}{\sigma_k} \Psi_k \chi_{k+1}^{(1)} dr = \frac{2r_{k+1} + r_k}{6\sigma_k}$$

$$\Theta_{kk+1}^{(1)} = \int_{r_k}^{r_{k+1}} r\xi_k \Psi_{k+1} dr = \frac{h_k}{6}(2r_{k+1} + r_k)$$

$$\Theta_{kk+1}^{(2)} = \int_{r_k}^{r_{k+1}} r\xi_{k+1} \Psi_k dr = 0$$

$$\Theta_{kk+1}^{(3)} = \int_{r_k}^{r_{k+1}} r\xi_k \chi_{k+1}^{(1)} dr = \frac{1}{6}(4r_{k+1}^2 + r_{k+1}r_k + r_k^2)$$

$$\Theta_{kk+1}^{(4)} = \int_{r_k}^{r_{k+1}} r\xi_{k+1} \chi_k^{(1)} dr = 0$$

$$\Theta_{kk+1}^{(5)} = \int_{r_k}^{r_{k+1}} r\xi_k \chi_{k+1}^{(2)} dr = r_{k+1}^2$$

$$\Theta_{kk+1}^{(6)} = \int_{r_k}^{r_{k+1}} r\xi_{k+1} \chi_k^{(2)} dr = 0$$

for $k' = k-1$ holds

$$
\begin{aligned}
K^{(3)}_{kk-1} &= \int_{r_k}^{r_{k+1}} \frac{1}{\sigma_k} \Psi_{k-1} \chi^{(1)}_k dr = \frac{2r_k + r_{k-1}}{6\sigma_{k-1}} \\
K^{(4)}_{kk-1} &= \int_{r_k}^{r_{k+1}} \frac{1}{\sigma_k} \Psi_{k} \chi^{(1)}_{k-1} dr = -\frac{r_k + 2r_{k-1}}{6\sigma_{k-1}} \\
\Theta^{(1)}_{kk-1} &= \int_{r_k}^{r_{k+1}} r \xi_k \Psi_{k-1} dr = 0 \\
\Theta^{(2)}_{kk-1} &= \int_{r_k}^{r_{k+1}} r \xi_{k-1} \Psi_{k} dr = \frac{h_{k-1}}{6}(2r_k + r_{k-1}) \\
\Theta^{(3)}_{kk-1} &= \int_{r_k}^{r_{k+1}} r \xi_k \chi^{(1)}_{k-1} dr = 0 \\
\Theta^{(4)}_{kk-1} &= \int_{r_k}^{r_{k+1}} r \xi_{k-1} \chi^{(1)}_{k} dr = \frac{1}{6}(4r_k^2 + r_k r_{k-1} + r_{k-1}^2) \\
\Theta^{(5)}_{kk-1} &= \int_{r_k}^{r_{k+1}} r \xi_k \chi^{(2)}_{k-1} dr = 0 \\
\Theta^{(6)}_{kk-1} &= \int_{r_k}^{r_{k+1}} r \xi_{k-1} \chi^{(2)}_{k} dr = r_k^2
\end{aligned}
$$

## A.5 Semi–analytical solutions

The semi–analytical benchmark solutions for the toroidal and poloidal case were respectively derived by Zdeněk Martinec and Jakub Velímský, and not published elsewhere. Here I summarize them with their permission.

We assume a two-layer conductivity model, so the EMI equation in the frequency domain (3.3) can be written as

$$
\left(\nabla^2 + k^2\right) \tilde{\mathbf{B}} = -\mu_0 \sigma \nabla \times \tilde{\mathbf{L}}, \tag{A.25}
$$

where $k = \sqrt{-\imath\omega\mu_0\sigma}$, in each of the layers, and with angular frequency $\omega = 2\pi/T$.

The eigenfunctions of the vector Helmholtz operator from equation (A.25) in the spherical domain are expressed using the vector spherical harmonics in lateral direction and complex spherical Bessel functions of complex argument of the first and second kind, $\mathrm{j}_j$ and $\mathrm{y}_j$, defined through their respective relations to the Bessel functions $\mathrm{J}_j$, $\mathrm{Y}_j$ as

$$
\mathrm{j}_j(x) = \sqrt{\frac{\pi}{2x}} \mathrm{J}_{j+\frac{1}{2}}(x), \qquad \textit{first kind} \tag{A.26}
$$

$$
\mathrm{y}_j(x) = \sqrt{\frac{\pi}{2x}} \mathrm{Y}_{j+\frac{1}{2}}(x). \qquad \textit{second kind} \tag{A.27}
$$

### A.5.1 Toroidal benchmark

We define the imposed electric field in the uppper layer and its rotation:

$$
\tilde{\mathbf{L}} = \sum_{jm} S_{jm} \left(\frac{r}{a}\right)^{j+1} \mathbf{Y}^{j+1}_{jm}, \tag{A.28}
$$

$$
\nabla \times \tilde{\mathbf{L}} = \frac{1}{a} \sum_{jm} S_{jm} \sqrt{\frac{j}{2j+1}} (2j+3) \left(\frac{r}{a}\right)^{j} \mathbf{Y}^{j}_{jm}. \tag{A.29}
$$

In the lower layer, there is no imposed electric field, so the EMI equation takes the form:

$$\left(\nabla^2 + k_B^2\right)\tilde{\mathbf{B}}_B = \mathbf{0}, \tag{A.30}$$

where $k_B = \sqrt{-\imath\omega\mu_0\sigma_B}$. In the ocean layer, the curl of the imposed electric field is present on the right–hand side

$$\begin{aligned}\left(\nabla^2 + k_A^2\right)\tilde{\mathbf{B}}_A &= -\mu_0\sigma_A\nabla\times\tilde{\mathbf{L}} \\ &= \frac{k_A^2}{\omega a}\sum_{jm} S_{jm}\sqrt{\frac{j}{2j+1}}(2j+3)\left(\frac{r}{a}\right)^j \mathbf{Y}_{jm}^j\,,\end{aligned} \tag{A.31}$$

where $k_A = \sqrt{-\imath\omega\mu_0\sigma_A}$.

Using spherical Bessel functions (A.26–A.27), analytical solutions for (A.30) and for (A.31) are

$$\begin{aligned}\tilde{\mathbf{B}}_A = \sum_{jm}\Big[&\alpha_{jm}\mathrm{j}_j(k_A r) + \beta_{jm}\mathrm{y}_j(k_A r) + \\ &+\frac{S_{jm}}{\omega a}\sqrt{\frac{j}{2j+1}}(2j+3)\left(\frac{r}{a}\right)^j\Big]\mathbf{Y}_{jm}^j,\end{aligned} \tag{A.32}$$

$$\tilde{\mathbf{B}}_B = \sum_{jm}\gamma_{jm}\mathrm{j}_j(k_B r)\mathbf{Y}_{jm}^j. \tag{A.33}$$

In the upper layer, the solution consists of the general solution with complex coefficients $\alpha_{jm}$ and $\beta_{jm}$, and the particular solution corresponding to the special choice of the forcing. In the lower layer, the spherical Bessel function of the second kind is absent, as it represents a non–physical solution, diverging for $r \to 0$.

We also need to derive the horizontal electric field in both layers, which is then used in the boundary condition across the layer interface,

$$\begin{aligned}\mathbf{e}_r\times\tilde{\mathbf{E}}_A &= \frac{1}{\mu_0\sigma_A}\mathbf{e}_r\times\nabla\times\tilde{\mathbf{B}}_A - \mathbf{e}_r\times\tilde{\mathbf{L}} = \\ &= \sum_{jm}\Bigg[-\frac{1}{\mu_0\sigma_A}\left(\frac{d}{dr}+\frac{1}{r}\right)\mathrm{j}_j(k_A r)\alpha_{jm} - \\ &-\frac{1}{\mu_0\sigma_A}\left(\frac{d}{dr}+\frac{1}{r}\right)\mathrm{y}_j(k_A r)\beta_{jm} + \\ &+\frac{\imath S_{jm}}{k_A^2 a^2}(2j+3)(j+1)\sqrt{\frac{j}{2j+1}}\left(\frac{r}{a}\right)^{j-1}\mathbf{Y}_{jm}^j - \\ &-\imath S_{jm}\sqrt{\frac{j}{2j+1}}\left(\frac{r}{a}\right)^{j+1}\Bigg]\mathbf{Y}_{jm}^j,\end{aligned} \tag{A.34}$$

$$\begin{aligned}\mathbf{e}_r\times\tilde{\mathbf{E}}_B &= \frac{1}{\mu_0\sigma_B}\mathbf{e}_r\times\nabla\times\tilde{\mathbf{B}}_B = \\ &= -\sum_{jm}\left[\frac{1}{\mu_0\sigma_B}\left(\frac{d}{dr}+\frac{1}{r}\right)\mathrm{j}_j(k_B r)\gamma_{jm}\right]\mathbf{Y}_{jm}^j.\end{aligned} \tag{A.35}$$

The coefficients $\alpha_{jm}, \beta_{jm}, \gamma_{jm}$ are determined from three boundary conditions:

1. $\tilde{\mathbf{B}}_A|_{r=a} = \mathbf{0}$ – boundary condition for the toroidal magnetic field on the surface

$$\alpha_{jm}\mathrm{j}_j(k_A a) + \beta_{jm}\mathrm{y}_j(k_A a) + \frac{S_{jm}}{\omega a}\sqrt{\frac{j}{2j+1}}(2j+3) = 0 \tag{A.36}$$

2. $\tilde{\mathbf{B}}_A|_{r=b} = \tilde{\mathbf{B}}_B|_{r=b}$ – continuity of the magnetic field $\tilde{\mathbf{B}}$ across the interface of layer A and B

$$\alpha_{jm}\mathrm{j}_j(k_A a)+\beta_{jm}\mathrm{y}_j(k_A a)+\frac{S_{jm}}{\omega a}\sqrt{\frac{j}{2j+1}}(2j+3)\left(\frac{b}{a}\right)^j = \gamma_{jm}\mathrm{j}_j(k_B b) \quad \text{(A.37)}$$

3. $\mathbf{e}_r \times \tilde{\mathbf{E}}_A|_{r=b} = \mathbf{e}_r \times \tilde{\mathbf{E}}_B|_{r=b}$ – continuity of the horizontal electric field across the interface of layer A and B

$$\left(\frac{1}{\mu_0\sigma_A}\mathbf{e}_r \times \nabla \times \tilde{\mathbf{B}}_A - \mathbf{e}_r \times \tilde{\mathbf{L}}\right)\Bigg|_{r=b} = \left(\frac{1}{\mu_0\sigma_B}\mathbf{e}_r \times \nabla \times \tilde{\mathbf{B}}_B\right)\Bigg|_{r=b}, \quad \text{(A.38)}$$

$$\begin{aligned}
&\frac{1}{\mu_0\sigma_A}\left(\frac{d}{dr}+\frac{1}{r}\right)\mathrm{j}_j(k_A r)\Big|_{r=b}\alpha_{jm}+\\
&+\frac{1}{\mu_0\sigma_A}\left(\frac{d}{dr}+\frac{1}{r}\right)\mathrm{y}_j(k_A r)\Big|_{r=b}\beta_{jm}-\\
&-\frac{\imath S_{jm}}{k_A^2 a^2}(2j+3)(j+1)\sqrt{\frac{j}{2j+1}}\left(\frac{b}{a}\right)^{j-1}+\\
&+\imath S_{jm}\sqrt{\frac{j}{2j+1}}\left(\frac{b}{a}\right)^{j+1} = \frac{1}{\mu_0\sigma_B}\left(\frac{d}{dr}+\frac{1}{r}\right)\mathrm{j}_j(k_B r)\Big|_{r=b}\gamma_{jm}.
\end{aligned} \quad \text{(A.39)}$$

By numerically evaluating the spherical Bessel functions and their derivatives, a system of three complex linear equations is assembled and solved by the Gauss elimination for the unknown coefficients $\alpha_{jm},\ \beta_{jm},\ \gamma_{jm}$.

### A.5.2 Poloidal benchmark

The imposed electric field and its rotation take the special forms,

$$\tilde{\mathbf{L}} = \sum_{jm} S_{jm}\left(\frac{r}{a}\right)^j \mathbf{Y}^j_{jm}, \quad \text{(A.40)}$$

$$\nabla \times \tilde{\mathbf{L}} = \frac{1}{a}\sum_{jm} S_{jm}\sqrt{(j+1)(2j+1)}\left(\frac{r}{a}\right)^{j-1}\mathbf{Y}^{j-1}_{jm}. \quad \text{(A.41)}$$

Again, we write the homogeneous vector Helmholtz equation for the magnetic field in the lower layer,

$$\left(\nabla^2 + k_B^2\right)\tilde{\mathbf{B}}_B = \mathbf{0}, \quad \text{(A.42)}$$

where $k_B = \sqrt{-\imath\omega\mu_0\sigma_B}$, and its inhomogeneous variant in the ocean layer,

$$\begin{aligned}
\left(\nabla^2 + k_A^2\right)\tilde{\mathbf{B}}_A &= -\mu_0\sigma_A\nabla\times\tilde{\mathbf{L}}\\
&= \frac{k_A^2}{\omega a}\sum_{jm} S_{jm}\sqrt{(j+1)(2j+1)}\left(\frac{r}{a}\right)^{j-1}\mathbf{Y}^{j-1}_{jm},
\end{aligned} \quad \text{(A.43)}$$

where $k_A = \sqrt{-\imath\omega\mu_0\sigma_A}$.

Each general solution now combines the spherical Bessel functions of order $j-1$ and $j+1$, and their respective spherical harmonic vectors. Again, a particular solution is added in the ocean layer, and non–physical diverging solution is excluded in the lower layer,

$$\tilde{\mathbf{B}}_A = \sum_{jm} \left[ \alpha_{jm}^{j-1} \mathrm{j}_{j-1}(k_A r) + \beta_{jm}^{j-1} \mathrm{y}_{j-1}(k_A r) + \frac{S_{jm}}{\omega a} \sqrt{(j+1)(2j+1)} \left(\frac{r}{a}\right)^{j-1} \right] \mathbf{Y}_{jm}^{j-1} + \sum_{jm} \left[ \alpha_{jm}^{j+1} \mathrm{j}_{j+1}(k_A r) + \beta_{jm}^{j+1} \mathrm{y}_{j+1}(k_A r) \right] \mathbf{Y}_{jm}^{j+1}, \tag{A.44}$$

$$\tilde{\mathbf{B}}_B = \sum_{jm} \left[ \gamma_{jm}^{j-1} \mathrm{j}_{j-1}(k_B r) \mathbf{Y}_{jm}^{j-1} + \gamma_{jm}^{j+1} \mathrm{j}_{j+1}(k_B r) \mathbf{Y}_{jm}^{j+1} \right]. \tag{A.45}$$

The divergence–free constraint on $\tilde{\mathbf{B}}$ allows to reduce the number of unknowns to 3 by substituting

$$\alpha_{jm}^{j+1} = -\sqrt{\frac{j}{j+1}} \alpha_{jm}^{j-1} \tag{A.46}$$

$$\beta_{jm}^{j+1} = -\sqrt{\frac{j}{j+1}} \beta_{jm}^{j-1} \tag{A.47}$$

$$\gamma_{jm}^{j+1} = -\sqrt{\frac{j}{j+1}} \gamma_{jm}^{j-1} \tag{A.48}$$

With that condition, equations can be rewritten

$$\tilde{\mathbf{B}}_A = \sum_{jm} \left[ \alpha_{jm}^{j-1} \mathrm{j}_{j-1}(k_A r) + \beta_{jm}^{j-1} \mathrm{y}_{j-1}(k_A r) + \frac{S_{jm}}{\omega a} \sqrt{(j+1)(2j+1)} \left(\frac{r}{a}\right)^{j-1} \right] \mathbf{Y}_{jm}^{j-1} - \sum_{jm} \sqrt{\frac{j}{j+1}} \left[ \alpha_{jm}^{j-1} \mathrm{j}_{j+1}(k_A r) + \beta_{jm}^{j-1} \mathrm{y}_{j+1}(k_A r) \right] \mathbf{Y}_{jm}^{j+1}, \tag{A.49}$$

$$\tilde{\mathbf{B}}_B = \sum_{jm} \left[ \gamma_{jm}^{j-1} \mathrm{j}_{j-1}(k_B r) \mathbf{Y}_{jm}^{j-1} - \sqrt{\frac{j}{j+1}} \gamma_{jm}^{j-1} \mathrm{j}_{j+1}(k_B r) \mathbf{Y}_{jm}^{j+1} \right]. \tag{A.50}$$

Auxiliary expressions of $\nabla \times \tilde{\mathbf{B}}$

$$\nabla \times \tilde{\mathbf{B}}_A = -\imath k_A \sum_{jm} \sqrt{\frac{2j+1}{j+1}} \left[ \alpha_{jm}^{j-1} \mathrm{j}_{j-1}(k_A r) + \beta_{jm}^{j-1} \mathrm{y}_{j-1}(k_A r) \right] \mathbf{Y}_{jm}^{j}, \tag{A.51}$$

$$\nabla \times \tilde{\mathbf{B}}_B = -\imath k_B \sum_{jm} \sqrt{\frac{2j+1}{j+1}} \gamma_{jm}^{j-1} \mathrm{j}_{j}(k_B r) \mathbf{Y}_{jm}^{j}, \tag{A.52}$$

are used in the description of electrical field,

$$\begin{aligned}\mathbf{e}_r \times \tilde{\mathbf{E}}_A &= \frac{1}{\mu_0 \sigma_A} \mathbf{e}_r \times \nabla \times \tilde{\mathbf{B}}_A - \mathbf{e}_r \times \tilde{\mathbf{L}} = \\ &= \frac{k_A}{\mu_0 \sigma_A} \sum_{jm} \left[ \alpha_{jm}^{j-1} \mathrm{j}_j(k_A r) + \beta_{jm}^{j-1} \mathrm{y}_j(k_A r) \right] \left[ \mathbf{Y}_{jm}^{j-1} + \sqrt{\frac{j}{j+1}} \mathbf{Y}_{jm}^{j+1} \right] - \\ &- \imath \sum_{jm} S_{jm} \left( \frac{r}{a} \right)^j \left[ \sqrt{\frac{j+1}{2j+1}} \mathbf{Y}_{jm}^{j-1} + \sqrt{\frac{j}{2j+1}} \mathbf{Y}_{jm}^{j+1} \right],\end{aligned} \tag{A.53}$$

$$\begin{aligned}\mathbf{e}_r \times \tilde{\mathbf{E}}_B &= \frac{1}{\mu_0 \sigma_B} \mathbf{e}_r \times \nabla \times \tilde{\mathbf{B}}_B = \\ &= \frac{k_A}{\mu_0 \sigma_B} \sum_{jm} \gamma_{jm}^{j-1} \mathrm{j}_j(k_B r) \left[ \mathbf{Y}_{jm}^{j-1} + \sqrt{\frac{j}{j+1}} \mathbf{Y}_{jm}^{j+1} \right].\end{aligned} \tag{A.54}$$

The coefficients $\alpha_{jm}^{j-1}, \beta_{jm}^{j-1}, \gamma_{jm}^{j-1}$ are determined from three boundary conditions:

1. $\tilde{\mathbf{B}}^{(ext)}|_{r=a} = \mathbf{0}$ – boundary condition for magnetic field $\tilde{\mathbf{B}}$

$$\alpha_{jm}^{j-1} \mathrm{j}_{j-1}(k_A a) + \beta_{jm}^{j-1} \mathrm{y}_{j-1}(k_A a) + \frac{S_{jm}}{\omega a} \sqrt{(j+1)(2j+1)} = 0 \tag{A.55}$$

2. $\tilde{\mathbf{B}}_A|_{r=b} = \tilde{\mathbf{B}}_B|_{r=b}$ – continuity for magnetic field $\tilde{\mathbf{B}}$ across the interface of layer A and B

$$\begin{aligned}&\alpha_{jm}^{j-1} \mathrm{j}_{j-1}(k_A a) + \beta_{jm}^{j-1} \mathrm{y}_{j-1}(k_A a) + \\ &+ \frac{S_{jm}}{\omega a} \sqrt{(j+1)(2j+1)} \left( \frac{b}{a} \right)^{j-1} = \gamma_{jm}^{j-1} \mathrm{j}_{j-1}(k_B b)\end{aligned} \tag{A.56}$$

$$\alpha_{jm}^{j-1} \mathrm{j}_{j+1}(k_A a) + \beta_{jm}^{j-1} \mathrm{y}_{j+1}(k_A a) = \gamma_{jm}^{j-1} \mathrm{j}_{j+1}(k_B b) \tag{A.57}$$

Note that the boundary condition $\mathbf{e}_r \times \tilde{\mathbf{E}}_A|_{r=b} = \mathbf{e}_r \times \tilde{\mathbf{E}}_B|_{r=b}$ is satisfied implicitly, and proof is left to a meticulous reader. (Hint: Take sum of two previous equations, and apply summation formulas for spherical Bessel functions.)

Again, a $3 \times 3$ complex linear system for unknown coefficeints $\alpha_{jm}^{j-1}$, $\beta_{jm}^{j-1}$, and $\gamma_{jm}^{j-1}$ is assembled and solved, using numerical values of spherical Bessel functions.